EVALUATION OF AN EXTREME-CONDITION-INVERSE CALIBRATION REMOTE SENSING MODEL FOR MAPPING ENERGY BALANCE FLUXES IN ARID RIPARIAN AREAS

Sung-ho Hong[1], Jan M.H. Hendrickx[2*], Jan Kleissl[3], Rick G. Allen[4], Wim G.M. Bastiaanssen[5], Russell L. Scott[6], Aaron L. Steinwand[7]

[1]Murray State University, Murray, KY; previously, New Mexico Tech, Socorro, NM; [2]New Mexico Tech, Socorro, NM; [3]University of California, San Diego, CA; [4]University of Idaho, Kimberly, ID; [5]Delft University of Technology and UNESCO-IHE, Delft, The Netherlands; [6]Southwest Watershed Research Center, USDA-ARS, Tucson, AZ; [7]Inyo County, Water Department, Independence, CA.

ABSTRACT

Accurate information on the distribution of the surface energy balance components in arid riparian areas is needed for sustainable management of water resources as well as for developing a better understanding of water and heat exchange processes between the land surface and atmosphere. Since the spatial and temporal distributions of these fluxes over large areas are difficult to determine from ground measurements, their prediction from remote sensing data is very attractive due to its large areal coverage and a high repetition rate. In this study the Surface Energy Balance Algorithm for Land (SEBAL) was used as a remote-sensing platform to estimate energy balance components in the arid riparian areas of the Middle Rio Grande Basin (New Mexico) and San Pedro Basin (Arizona), and areas of phreatophytic shrubs and grasses in the Owens Valley (California). We compared instantaneous and daily fluxes from SEBAL derived from Landsat TM images to surface-based measurements from eddy covariance flux towers. This study presents evidence that inversion-calibrated surface energy balance models

[*] Corresponding author: janhendrickxnmt@gmail.com

such as SEBAL and similar models such as METRIC can yield reliable estimates for actual evapotranspiration rates in riparian areas of the southwestern United States. The great strengths of the inversion-calibrated methods are their internal calibration strategies that eliminate much of the effects of systematic biases in net radiation, soil heat flux, land surface temperature and albedo on latent heat flux, at the expense of increased bias in sensible heat flux.

1. INTRODUCTION

The regional distribution of the energy balance components, net surface radiation (R_n), soil heat flux (G), sensible heat flux (H) and latent heat flux (LE) in arid riparian areas is critical knowledge for agricultural, hydrological and climatological investigations. However, R_n, G, H and LE are complex functions of atmospheric conditions, land use, vegetation, soils, and topography which cause these fluxes to vary in space and time. It is difficult or impractical to estimate surface fluxes at the regional scale using ground-based instruments (Parlange et al., 1995). Measurement approaches for LE from the land surface such as eddy covariance (Kizer and Elliott, 1991), Bowen ratio (Scott et al., 2004) and weighing lysimeters (Wright, 1982) are too expensive and time consuming for continuous application at sufficient spatial density at regional scales. These techniques produce LE measurements over small footprints (m^2 to ha) which are difficult to extrapolate to the regional scale, especially over heterogeneous land surfaces (Moran and Jackson, 1991). For example, in the heterogeneous landscape of the central plateau of Spain as many as 13 ground measurements of evapotranspiration in a relatively small area of 5000 km^2 were not sufficient to predict accurately the area-averaged evapotranspiration rate (Pelgrum and Bastiaanssen, 1996).

A number of studies have concluded that reliable regional estimates of spatial patterns of *LE* can be obtained by satellite image-based remote sensing algorithms (e.g. Choudhury, 1989;Granger, 2000;Moran and Jackson, 1991;Kustas and Norman, 1996;Du et al., 2013). A variety of *LE* remote sensing algorithms exists with different spatial (30 m to 1/8th degree or 13 km in New Mexico) and temporal (daily to monthly) scales. Examples include: the Two-Source Energy Balance model (TSEB) (Norman et al., 1995), the Hybrid dual source Trapezoid framework Evapotranspiration Model (HTEM) (Yang and Shang, 2013), the Atmosphere-Land Exchange Inverse (ALEXI) (Anderson et al., 1997), the disaggregated ALEXI model (DisALEXI) (Norman et al., 2003), the Surface Energy Balance System (SEBS) (Su, 2002), the MOD16 ET algorithms (Mu et al., 2011), the Simplified Surface Energy Balance (SSEB) (Senay et al., 2013), the Surface Energy Balance Algorithm for Land (SEBAL) (Bastiaanssen, 1995), Mapping EvapoTranspiration at high spatial Resolution with Internalized Calibration (METRIC) (Allen et al., 2007), as well as algorithms without distinct acronyms (Schüttemeyer et al., 2007;Ma et al., 2004;Jiang and Islam, 2001).

SEBAL was developed by Bastiaanssen and his colleagues in The Netherlands during the 1990s (Bastiaanssen, 1995). METRIC was developed by Allen and his research team in Idaho using SEBAL as its foundation (Allen et al., 2005), but with greater reliance on weather-based reference ET calculations for calibration. SEBAL and METRIC do not require spatial fields of air temperature and atmospheric temperature soundings interpolated across the region of interest like ALEXI and DisALEXI. SEBAL and METRIC do not require land cover maps for estimating surface roughness but instead can use expressions that relate the NDVI to the momentum roughness length (Bastiaanssen et al., 1998a;Allen et al., 2007). However, SEBAL and METRIC are restricted to clear days over areas of stable weather and generally require some supervised calibration for each image. These requirements limit their application to local and regional scale, rather than at continental scale that is possible with ALEXI, SSEB, or MOD16. Interpolation of ET between images is done using ground-based or gridded reference ET and interpolated fractions of reference ET.

The accuracy of SEBAL and METRIC for evaporation mapping worldwide is typically about ±15% for daily and ±1-5% for seasonal evaporation estimates (Bastiaanssen et al., 2005;Allen et al., 2011;Karimi and Bastiaanssen, 2015). Accuracy of the models depends on a calibration method that selects a “cold” and “hot” pixel representing extreme thermal and vegetation conditions within an image. After calculation of the energy balance at the two calibration pixels, the near-surface air temperature gradient associated with sensible heat flux H for each pixel is indexed to its satellite measured surface temperature.

The economic efficiency of SEBAL and METRIC is particularly attractive. For example, in the early 1980’s co-author Hendrickx with a team of field assistants and graduate students spent two years in the Office du Niger (Mali) to measure the seasonal actual evapotranspiration of rice in four irrigation units encompassing an area of about 70 hectares using non-weighing lysimeters and discharge measurements in irrigation and drainage ditches (Hendrickx et al., 1986). For comparison, in 2008, the seasonal actual evapotranspiration was obtained by two scientists, (Zwart and Leclert, 2010), for 86,000 hectares from the Office du Niger using SEBAL with Landsat imagery of 2006 in approximately two months. The economy of the method justifies further investigations to validate the SEBAL model for a variety of field environments.

Previous validation studies of SEBAL have been conducted in relatively homogeneous agricultural areas and have focused on a comparison of daily ET rates estimated from SEBAL (or METRIC) with ground measurements using lysimeters (Tasumi, 2003;Trezza, 2002), Bowen ratio and eddy covariance methods (Gibson et al., 2013;Du et al., 2013;Bastiaanssen et al., 2002) and scintillometry (Hemakumara et al., 2003;Kite and Droogers, 2000;Kleissl et al., 2009). The overall goal of this study was to conduct a thorough evaluation of the performance of SEBAL in arid riparian areas in New Mexico, Arizona and California where spatially extensive estimates of the ground and surface water balance components are needed to improve land and water management. The study areas include vast deserts transected by relatively narrow river corridors and a mosaic of irrigated agricultural fields and riparian vegetation (cottonwood, saltcedar, willow, mesquite, Russian olive) and native phreatophytic shrubs and grasses which creates a very heterogeneous landscape with a short patch length scale. A good SEBAL performance under these challenging conditions would be a strong indication that satisfactory performance should be expected from other types of moderate to high ET systems that are surrounded by relatively dry land uses (e.g. Compaoré et al., 2008).

This study involves SEBAL applications in areas without high quality hourly meteorological observations which represents a common condition for many regions worldwide (Droogers and Allen, 2002). We examined each component of the energy balance during the instant of satellite overpass and on a daily basis using a quality controlled data set consisting of ground-based R_n, H and LE measurements.

2. SURFACE ENERGY BALANCE ALGORITHM FOR LAND (SEBAL)

SEBAL is a remote sensing algorithm that evaluates the fluxes of the energy balance and determines *LE* as the residual

$$LE = (1-\alpha)R_s + R_{l\_in} - R_{l\_out} - (1-\varepsilon_o)R_{l\_in} - G - H = R_n - G - H \quad [1]$$

where R_s is the incoming shortwave radiation [Wm^{-2}], α is the surface albedo [-], R_{l_in} is the incoming longwave radiation [Wm^{-2}], R_{l_out} is the emitted longwave radiation [Wm^{-2}], ε_o is the surface thermal emissivity [-]R_n [Wm^{-2}], *G* is the soil heat flux density [Wm^{-2}], *H* is the sensible heat flux density [Wm^{-2}], *LE* (= λET) is the latent heat flux density [Wm^{-2}], and R_n is the net radiation flux density [Wm^{-2}]. *LE* can be converted to the ET rate [$mmday^{-1}$] using the latent heat of vaporization of water λ [Jkg^{-1}] and the density of water ρ_w [kgm^{-3}].

To implement SEBAL, images must include information on reflectance in the visible, near-infrared, mid-infrared bands, and emission in the thermal infrared band. The necessary data are available from a number of satellites including Land Satellite (Landsat), Moderate Resolution Imaging Spectroradiometer (MODIS), Advanced Very High Resolution Radiometer (AVHRR), Advanced Spaceborne Thermal Emission and Reflection Radiometer (ASTER), ENVISAT-Advanced Along Track Scanning Radiometer (AATSR) and China-Brazil Earth Resources Satellite (CBERS). In this study, we use Landsat images for their high spatial resolution and consistent, accurate calibration. A digital elevation model (DEM) is used to account for terrain slope and aspect of each pixel. Extensive descriptions of SEBAL and METRIC have been presented in the literature (Allen et al., 2011;Allen et al., 2007;Hong, 2008;Bastiaanssen et al., 1998a). Critical elements of the SEBAL algorithm are discussed below.

R_n and G are determined using standard approaches similar to other energy balance remote sensing algorithms, but SEBAL and METRIC have a different unique method for the estimation of the sensible heat flux density (H). The traditional aerodynamic equation for H is between surface and air temperature measurement height (Brutsaert et al., 1993)

$$H = \frac{\rho_a \cdot c_p \cdot (T_{aero} - T_a)}{r_{ah}} \quad [2]$$

where ρ_a is the density of air [kgm^{-3}], c_p is the specific heat capacity of air [Jkg^{-1}K^{-1}], T_{aero} is the aerodynamic surface temperature, T_a is the air temperature measured at a standard screen height, and r_{ah} is the aerodynamic resistance to heat transfer [sm^{-1}] between the surface and air temperature measurement height. SEBAL and METRIC overcome the challenge of inferring the aerodynamic surface temperature from the radiometric surface temperature and the need for near-surface air temperature measurements by directly estimating the temperature difference ΔT between T_1 and T_2 taken at two levels z_1 (0.10 m) and z_2 (2 m) above the canopy or soil surface without calculation of the absolute temperature at any given height.

$$H = \frac{\rho_a \cdot c_p \cdot \Delta T}{r_{ah12}} \quad [3]$$

where r_{ah12} is the aerodynamic resistance between levels z_1 and z_2. The ΔT gradient essentially ‘floats’ over the surface. The temperature difference for a dry surface without evaporation (the hot pixel) is obtained from the energy balance equation (Eq. [1]) with LE assumed to be zero so that $H = R_n - G$ followed by the inversion of Eq. [3] to $\Delta T = H\, r_{ah12}/(\rho_a\, c_p)$. LE is set to a positive value during calibration if a daily soil water process model using precipitation inputs reveals residual evaporation from prior precipitation events. For a wet surface (the cold pixel) all available energy $R_n - G$ is assumed to be used for evapotranspiration so that $H = 0$ and $\Delta T = 0$ (Bastiaanssen et al., 1998a;Bastiaanssen, 2000). In METRIC, H at the cold pixel is estimated as $H = R_n - G - ET_{cold}$ where ET_{cold} is assigned a value based on scaled weather-based reference ET. The implicit assumption in extreme-condition-inverted-calibration processes such as SEBAL and METRIC is that land surfaces with a high ΔT are associated with high radiometric temperatures and those with a low ΔT are associated with low radiometric temperatures. Field measurements in Egypt and Niger (Bastiaanssen et al., 1998b), China (Wang et al., 1998), and USA (Franks and Beven, 1997) have shown that the relationship between T_s and ΔT is positive and approximately linear for a variety of field conditions including irrigated fields, deserts and mountains.

$$\Delta T = c_1 \cdot T_s + c_2 \tag{4}$$

where c_1 and c_2 are the linear regression coefficients valid for a landscape at the time and date the image is taken. By using the values of ΔT calculated for the cold and hot pixel, the regression coefficients c_1 and c_2 can be determined so that the extremes of H are constrained and outliers of H-fluxes are prevented. Equation [4] is dependent upon spatial differences of the radiometric surface temperature rather than absolute surface temperatures to derive maps of the sensible heat flux which minimizes the need for atmospheric corrections as well as uncertainties in surface emissivity, surface roughness and differences in T_{aero} and T_s on H estimates (Allen et al., 2007).

Besides ΔT the other unknown in Eq. [3] is the aerodynamic resistance to heat transfer (r_{ah12}), which is affected by wind speed, atmospheric stability, and surface roughness. Because r_{ah12} and H are interdependent, an iterative process is used to calculate H (Allen et al., 2007;Hong, 2008). After inserting R_n, G and calculated H into Eq. [1] the latent heat flux LE is obtained for each pixel. Finally, dividing *LE* by the latent heat of vaporization of water yields the instantaneous ET (mmhour^{-1}) at the time of the Landsat overpass.

SEBAL and METRIC produce an estimate of the instantaneous *LE* at the time of the satellite overpass at approximately 10:30 am. However, for most hydrological applications the daily *LE* is needed, and the instantaneous *LE* must be extrapolated to estimate the daily *LE* using the instantaneous evaporative fraction (EF_{inst}). Where daily soil moisture does not significantly change and advection does not occur, the evaporative fraction has been shown to be approximately constant during the day (Crago, 1996;Farah et al., 2004). However, analysis of field measurements by other investigators (Teixeira et al., 2008;Anderson et al., 1997;Sugita and Brutsaert, 1991) indicates that the instantaneous evaporative fraction on clear days at satellite overpass time tends to be approximately 10 – 18 % smaller than the daytime average. Therefore, a correction coefficient c_{EF} is introduced to take into account differences between instantaneous and daily evaporative fractions. Some investigators use c_{EF} of 1.00 (Bastiaanssen et al., 2005) while others suggest c_{EF} of 1.10 (Anderson et al., 1997) or c_{EF} of 1.18 (Teixeira et al., 2008). The value for c_{EF} should depend on the relative amount of advection of heat, which in turn is a function of regional evaporation, wind speed and relative humidity.

$$EF_{inst} \cdot c_{EF} = \frac{R_n - G - H}{R_n - G} \cdot c_{EF} = \frac{LE_{inst}}{LE_{inst} + H_{inst}} \cdot c_{EF} = EF_{24} = \frac{\lambda \cdot \rho_w \cdot ET_{24}}{R_{n24} - G_{24}} \cdot c_{EF} \qquad [5]$$

Assuming daily soil heat flux G_{24} [MJm^{-2}day^{-1}] close to zero, multiplication of the instantaneous EF_{inst} determined from SEBAL with the total daily available energy yields the daily ET rate in mm per day (Bastiaanssen et al., 1998a)

$$ET_{24} = \frac{c_{EF} EF_{inst} \cdot (R_{n24} - G_{24})}{\lambda \cdot \rho_w} \approx \frac{c_{EF} EF_{24} \cdot R_{n24}}{\lambda \cdot \rho_w} \qquad [6]$$

where ET_{24} is daily ET [mm day^{-1}], ρ_w is the density of water [k gm^{-3}] and R_{n24} is daily net radiation [MJm^{-2}day^{-1}] obtained by an semi-empirical expression (De Bruin, 1987) as described by (Hong, 2008). Finally, the daily H_{24} is not derived from the instantaneous H but is calculated as the difference between R_{n24} and LE_{24}.

3. METHOD AND MATERIALS

3.1. Study Areas

The components of the energy balance (R_n, G, H and LE) were determined using a SEBAL version having R_n and G components similar to those of METRIC (Allen et al., 2005). The SEBAL model was applied to sixteen Landsat 7 images from 2000 to 2003 for three typical desert phreatophyte and riparian areas in the southwestern United States located in the Middle Rio Grande Valley (NM), the Owens Valley (CA) and the San Pedro Basin (AZ). (Figure 1, Table 1)

The Middle Rio Grande Valley extends through central New Mexico and is defined as the reach of the Rio Grande between Cochiti Dam and Elephant Butte Reservoir. The Middle Rio Grande riparian vegetation consists of cottonwood and salt grasses as well as various non-native species including saltcedar and Russian olive. In the Middle Rio Grande Valley, the average annual air temperature is 15 °C. Daily summer temperatures range from 20 to 40 °C, and daily winter temperatures range from -12 to 10 °C. Mean annual precipitation is about 25 cm and mean annual potential evapotranspiration is approximately 170 cm.

The Owens Valley is a long, narrow valley on the eastern slope of the Sierra Nevada in Inyo County, California. It is a closed basin drained by the Owens River which terminates at saline Owens Lake playa. The Owens Valley has a mild high-desert climate: in summer (June, July and August) the lowest average daily minimum temperature is 7 °C and the highest average daily maximum temperature temperatures is 37 °C, in winter (November to February) temperature varies between -7 to 21 °C. Since, the Owens Valley is located in the rain shadow of the Sierra Nevada, the average annual precipitation in the Owens Valley is only about 12 cm and mean annual potential evapotranspiration is about 150 cm. Snowmelt runoff from the Sierra Nevada creates a shallow water table underneath the valley floor which supports approximately 28,000 hectares of native phreatophytic shrubs and grasses and riparian areas.

The San Pedro Basin begins in Sonora, Mexico and extends to the Gila River in southern Arizona. The San Pedro River is surrounded by vegetation consisting of cottonwood, willow, mesquite and sacaton grass. The mean air temperature is around 18 °C. Daily summer temperatures range from 22 to 44 °C, while daily winter temperatures range from 9 to 24 °C. Mean annual precipitation is about 35 cm and mean annual potential evapotranspiration is approximately 170 cm.

Although the regional climate of all three areas is classified as arid/semiarid, the study areas have different precipitation patterns. In the Owens Valley, precipitation occurs primarily in winter and spring, while in the San Pedro and the Middle Rio Grande Valleys, the annual precipitation distribution is bimodal with more than half of the rainfall being monsoonal in summer, although the proportion varies considerably from year to year (Cleverly et al., 2002;Elmore et al., 2002;Scott et al., 2000;Stromberg, 1998;Costigan et al., 2000). Table 2 presents main characteristics of the study sites.

3.2. Eddy Covariance Measurements and Closure Forcing

At each site, the turbulent heat fluxes were measured using the eddy covariance (EC) method that theoretically provides direct and reliable measurements of *H* and *LE* (Arya, 2001). At all sites, a three-dimensional sonic anemometer-thermometer that measured the three-dimensional wind vector and virtual temperature was collocated with a Krypton hygrometer or open path infrared gas analyzer that measured water vapor density [gm^{-3}] with a sampling rate of 10 Hz (Cleverly et al., 2002;Steinwand et al., 2006;Scott et al., 2004). Covariance between the vertical wind speed and water vapor density and virtual air temperature were used to compute 30 minutes averages of *LE* and *H*. The eddy covariance systems were oriented toward the predominant wind direction to reduce interference from winds blocked by the tower and instrumentation. All eddy covariance data were quality controlled and corrected for tilt by coordinate rotations, frequency response, oxygen absorption of the Krypton hygrometer, and flux effects on air density. The coordinate rotation, however, cannot correct for changing wind direction during 30-minute average periods which can cause mean vertical wind speeds to deviate from 0, thereby inducing error in the *H* and *LE* measurements. This problem is common to EC measurements in tall vegetation such as trees when the sensors are placed too close to tree branches or canopy. Soil heat fluxes in the San Pedro Valley and Owens Valley were obtained from soil heat flux plates that were corrected for soil heat storage above the plate using collocated soil temperature and soil moisture measurements.

At the Middle Rio Grande sites, soil heat storage could not be calculated due to the absence of soil moisture measurements. Therefore, the soil heat flux measurements for those sites were not compared with SEBAL estimates. Net radiation was obtained from REBS Q7 or

Kipp and Zonen CNR1 net radiometers. To compare the 30-minute average ground measurements with the instantaneous energy fluxes estimated using SEBAL, an instantaneous ground measurement was determined by linear interpolation between the 30 minutes periods before and after the satellite overpass. Daily values of LE, H, G and R_n were derived by summing the 30 minutes fluxes through the day (00 – 24 hours).

We used the relative closure of the energy balance (Twine et al., 2000) as a criterion to filter the datasets to select only high-quality R_n, G, H, and LE ground measurements for comparison with SEBAL estimates. Figure 2 presents the relative closures calculated for satellite overpass days for all sites as provided by the investigators operating the EC towers in the Owens and San Pedro River Valleys. Since no soil heat flux measurements were available in the Middle Rio Grande Valley, we calculated the instantaneous relative closure [%] using the instantaneous soil heat flux derived by SEBAL instead of the ground measured soil heat flux. This approach was justified on the basis of the reasonable agreement found between SEBAL derived instantaneous soil heat fluxes and those measured on the ground in the Owens and San Pedro River Valleys (discussed below). If the sum of H and LE, before correction, was less than 65 % or greater than 110 % of the available energy ($R_n – G$), the data were not used in our analysis. (Wilson et al., 2002) found the average energy balance closure at FLUXNET sites to be between 53 to 99%. Since their numbers represent average closures and since data points at the lower end of the range raise greater concerns for data quality, we chose to shift the range up. Our criterion excluded 45 % of instantaneous fluxes and 39 % of the daily fluxes of the data from the Middle Rio Grande Valley, 79 % (instantaneous) and 43 % (daily) from the Owens Valley and 17 % (instantaneous) and zero % (daily) from the San Pedro River Valley. The remaining turbulent heat flux estimates were improved through forcing the closure of the energy balance by increasing *LE* and *H* by the Bowen ratio (Twine et al., 2000). The improved adjusted *H* and *LE* are identified as H_{adj} and LE_{adj}.

After elimination of EC measurements on the basis of unacceptable closures, we eliminated also the EC measurements taken on May 16, 2003 in the San Pedro River Valley at the Mesquite (CM) site because the wind direction differed considerably from the prevailing wind direction and was from a direction with very limited upwind fetch (<100 m). The problem was exacerbated by the relatively high placement (7 m) of the sensors above the canopy (Table 2) since the heat fluxes can vary significantly with height under such conditions (De Bruin et al., 1991).

3.3. Scale Differences of SEBAL Flux Predictions and Ground Measurements

Comparison of remotely sensed (RS)-derived estimates of R_n, *G*, *H* and *LE* with ground measurements is not straightforward because the spatial and temporal scales of the RS predictions and ground measurements are quite different. In this section we will discuss the effects of these scale differences on each flux in the energy balance.

3.3.1. Net radiation

R_n is measured with a net radiometer at a height of about 2 – 3 m above the canopy (Table 2) that covers typically an observation area on the order of 10 m^2. The RS-based R_n estimate is derived from reflectance in the visible, near-infrared and mid-infrared bands from a 900 m^2 pixel as well as the emittance in the thermal band from a 3600 m^2 pixel. Details of the algorithms used are given in Allen et al. (2007) and are common to many applications of SEBAL and METRIC. The R_n ground observation is based on a measurement area at least two orders of magnitude smaller than the RS-based prediction. For homogeneous areas the scale difference affects the comparison of ground and satellite measurements little, but for heterogeneous areas it may cause serious bias. Satellite based R_n samples a larger area and is therefore more representative of the landscape within the footprint of the eddy covariance instrument. In riparian areas, sparse vegetation with open canopies and vegetation gradients perpendicular to the river channel create a heterogeneous landscape. Radiometers are typically placed over the canopy of interest which may under-represent surrounding bare soil or ground cover within the angle of view. As a result, ground measured R_n may be biased towards the R_n of the specific vegetation.

3.3.2. Soil heat flux

G was measured by soil heat flux plates combined with changes in heat storage above the plate using soil temperature and soil water content measurements. If *G* is not corrected for heat storage above the plate, large errors will result (Sauer, 2002a). The measurement area of a soil heat flux plate is about 0.001 m^2 which is almost six orders of magnitude less than a 900 m^2 Landsat pixel. The instantaneous *G* can vary widely depending on soil condition (20 – 300 Wm^{-2}), so that numerous flux measurements would be needed to estimate the average pixel *G* with the desired accuracy (Kustas et al., 2000;Humes et al., 1994). Therefore, we expect the instantaneous *G* ground measurements to be a rather crude estimation of the true instantaneous *G* at the scale of the pixel (Sauer et al., 2003). The impact of the scale difference on the comparison of ground and satellite measurements is somewhat mitigated by the fact that instantaneous *G* is positive during the day and negative during the night. Consequently, daily *G* is small compared to the other components of the energy balance (Seguin and Itier, 1983).

3.3.3. Sensible and latent heat fluxes

At all three sites *H* and *LE* were measured using a three-dimensional sonic anemometer-thermometer and a krypton hygrometer, or open patch infrared gas analyzer. For these components of the energy balance the area of ground measurements is often several times larger than a Landsat pixel. A typical footprint for *H* and *LE* under clear sky micrometeorological conditions covers about 5 pixels or about 4500 m^2. The location of the footprint is upwind of the EC tower, and its size depends on atmospheric stability. In the comparison of RS-based *H* and *LE* estimates with ground measurements, the footprint area must be estimated and the weighted average RS-estimated *H* and *LE* is computed for pixels within the footprint area. This approach is expected to work reasonably well for comparison of RS-based instantaneous *H* and *LE* estimates with ground measurements at the time of the satellite overpass.

Comparison of daily *H* and *LE* fluxes is problematic. Therefore, rather than trying to determine the true location of the “representative” daily foot print, the daily *H* and *LE* ground measurements are compared with the average RS-estimated *H* and *LE* fluxes originating from twenty-four homogeneous pixels surrounding the EC tower. The homogeneity of the pixels surrounding the tower was evaluated by inspecting NDVI, albedo, and surface temperature values as well as the *H* and *LE* values themselves.

3.3.4. Quantitative measures to compare SEBAL estimates and ground measurements

The numerical comparison of the energy balance components (R_n, *G*, *H*, and *LE*) estimated from RS with those measured on the ground was conducted by means of quantitative measures proposed by Willmott and others for the validation of atmospheric models (Willmott, 1981;Fox, 1981;Willmott, 1982). We examined the coefficient of determination (r^2), mean absolute difference (MAD), root mean square difference (RMSD), and the mean relative difference (MRD) (Hong, 2008). A high or statistically significant r^2 can be misleading because its values are often unrelated to the magnitude of the differences between model estimates and measurements (Willmott and Wicks, 1980). In addition, the distributions of the estimates and measurements often do not fulfill the assumptions of inferential statistics (Willmott, 1982). However, since r^2 is a commonly used correlation measure that reflects the proportion of the variance explained by the model, we report this measure. The MAD and RMSD are robust measures as they summarize the mean differences between SEBAL estimates and ground measurements; the MAD is less sensitive to outliers than RMSD. The MRD is often used as an indication how well RS-based estimates agree with ground measurements (Bastiaanssen et al., 2005).

3.4. Footprint Model

The location and extent of the footprint depends on surface roughness, atmospheric stability, wind speed, wind direction and may cover many pixels upwind of the eddy covariance tower (Schmid and Oke, 1990;Hsieh et al., 2000). The footprint flux, $F_{(x, Zs)}$ [-], along the upwind direction, x [m], measured at the height z_s [m], suggested by (Hsieh et al., 2000) was used in this study.

A typical footprint size and footprint intensity for one 30 minute period on August 19, 2002, at a Rio Grande saltcedar EC tower is presented in Figure 3. To verify the quality of the footprint model used in this study, we also calculated the location of maximum contribution to the measured flux (x_{max}) for this period with the model by Schuepp et al. (1990) . The models by Hsieh et al (2000) and Schuepp et al. (2000) calculate x_{max} as 10 m (Figure 3) and 11 m, respectively, which implies that the footprint from Hsieh et al (2000) is indeed close to the tower. At most EC sites, the maximum contribution to the footprint was within 50 m from the tower (wind speeds were generally less than 4 ms^{-1}) and most of the footprint intensity (>90 %) is located within 300 m from the tower. Approximately 80 % of all footprint fluxes cover an area of 5 to 9 pixels, twenty percent cover larger areas. Because calculation of a representative daily footprint for *H* and *LE* is nearly impossible, the average RS daily *H* and *LE* values of the 24 pixels surrounding the EC tower pixel are used for comparison with daily ground measurements.

3.5. Calibration and Evaluation of RS-based Flux Predictions

The temperatures of the cold and hot pixel for the derivation of calibration coefficients c_1 and c_2 in Eq. [4] are critical in SEBAL and METRIC because they constrain *LE* between its maximum value at the cold wet pixel and near zero at the hot dry pixel. The coefficients also incorporate and compensate for bias in *H* associated with uncertainties in aerodynamic characteristics including T_s (Bastiaanssen et al., 2005;Allen et al., 2006). In SEBAL and METRIC this calibration is entirely based on information available within the image and is variously referred to as self-calibration (Bastiaanssen et al., 2005) or internalized calibration and autocalibration.

At the cold pixel it is assumed in SEBAL that $\Delta T = 0$, which implies that $H = 0$ and $LE =$

$R_n - G$. An alternative manner in METRIC is to use hourly meteorological observations for the calculation of the reference ET (Allen et al., 1998) for the estimation of *H* in well-irrigated alfalfa or clipped grass fields (Allen et al., 2007;Allen et al., 2011). However, this study deals with a SEBAL application to riparian areas without high quality hourly meteorological observations as is the default condition for many regions worldwide (Droogers and Allen, 2002). The selection of the hot pixel is challenging because the heterogeneous landscapes of the southwestern U.S. include hot and dry areas with a wide range of temperatures. In this study, the hot pixel was selected from a dry bare agricultural field where ET can reasonably be assumed to be near zero. Any pixel cooler than the selected hot pixel has ET > 0 (if the R_n and *G* are the same), and for any pixel warmer than the hot pixel, for example parking lots, ET = 0. In addition, the equation to estimate *G* was derived for agricultural conditions and therefore produces more dependable estimates for calibration when applied to a bare, agricultural soil having a tillage history.

As a consequence of the internalized calibration, bias in R_n or *G* at the hot pixel in the image are transferred into *H*. However, the bias is present in both $R_n - G$ and *H* (Eq. [1]), and thus cancels out in the calculation of *LE* (Allen et al., 2006). The internalized calibration results in the least biased *LE* if the cold and hot pixel are properly selected and is the most distinctive feature of SEBAL and METRIC compared to other remote sensing *LE* algorithms.

The selection of cold and hot pixel is assisted by a thorough understanding of field micrometeorology and is somewhat subjective. (Kleissl et al., 2009) proposed using micrometeorological ground measurements of energy balance components for the calibration and validation of remote sensing algorithms. However, due to the relatively large uncertainties of ground measured sensible and latent heat fluxes (Loescher et al., 2005;Kleissl et al., 2008) the value of using ground measurements for calibration of SEBAL is not well established. We tested two different calibration approaches for the selection of the temperatures for the cold and hot pixel: the Empirical (EM) approach and the Eddy Covariance (EC) approach. The former selects the cold and hot pixel by inspection of the hydrogeological features of the landscape and qualitative micrometeorological considerations and is typical for most SEBAL applications. The Eddy Covariance (EC) approach is based on inspection of the hydrogeological features of the landscape followed by fine-tuning the parameters c_1 (slope) and c_2 (intercept) in Eq. [4] using ground measurements of instantaneous latent heat fluxes at the EC towers after adjustment for energy balance closure. This approach is viable because of the large number of ground based measurements in this study. The temperature of the cold pixel was fixed by selecting a pixel in fully vegetated fields, but the selection and temperature of the hot pixel was varied to best match the instantaneous ground measurements of *LE* (Hong, 2008).

Five different calibration scenarios (S1 – S5) were compared (Table 3). In the EC approach, calibration of SEBAL to ground measurements was implemented either using the average footprint weighted instantaneous SEBAL *LE* heat fluxes (S1, EC_FP) or using the instantaneous SEBAL *LE* heat flux of the pixel where the EC tower was located (S2, EC_TP). The former method is difficult to implement for most practitioners while the latter is practical and fast but requires homogeneous conditions around the tower within the maximum extent of the footprint. The EM approach (S3) was implemented without using the *LE*'s measured by the EC towers or any other meteorological measurements. In Section [3.3.1] we hypothesized that the ground measured R_n may be biased towards vegetation while the SEBAL R_n may be more representative for the true R_n of a pixel covered with vegetation and bare soil patches. Initial results suggested that the (SR_n) is more representative than ground R_n. Therefore, we also evaluated the impact of using the more accurate SR_n for energy balance closure in the EC approach on the tower pixel (S4, EC_TP/SR_n) and in the EM approach (S5, SR_n).

4. RESULTS AND DISCUSSION

4.1. Spatio-temporal Distribution of Daily Latent Heat Fluxes

Figure 4 presents an example of daily ET rates in the Middle Rio Grande Valley and surrounding desert on four different days during the spring, summer and fall. The maps show how the ET rates increase from April 7 (just after the start of the irrigation season) to June 16 at the height of the irrigation season; a decrease of ET is observed during September and October when fields were harvested and lower temperatures impede crop growth. On all four days higher ET rates were observed over irrigated fields and in the riparian areas while low to zero rates occurred in the surrounding desert.

4.2. Comparison of RS-Based Net Radiation with Ground Measurements

Figures 5 and 6 and Table 4 present the comparisons of the instantaneous and daily R_n measured on the ground and estimated by SEBAL. MADs for the EC approaches (S1/S2) and Empirical Approach (S3) were 88/87 and 97 W/m^2, respectively; MRDs were 13.0/12.8 and 14.6%. These differences are about two to three times larger than those typically reported for SEBAL (Jacob et al., 2002;Allen et al., 2006). The much larger MRD was attributed to the heterogeneity of the riparian sites and the different footprints of net radiometer and Landsat pixel

(Section [3.3.1]). Higher net radiation measured on the ground compared with the RS-based R_n supports this argument. The MRDs of 9.2 and 17.2 % from (Su, 2002) on heterogeneous pixels of shrub and grassland vegetation are similar to the ones reported in this study (Table 4).

Contrary to the instantaneous values, the daily net radiation measured on the ground and determined in SEBAL match very well (MRDs of -2.3 to -2.9%). This immediately begs the question "why?" since the instantaneous R_n differ by more than 12%. On clear days over sparsely vegetated surfaces the maximum temperature difference between bare soil and vegetation typically occurs around noon. For example, temperature differences measured in the Walnut Gulch Experimental Watershed near Tombstone, Arizona, varied between 10 and 25 ºC during that time of the day (Humes et al., 1994). Since the conditions in the arid riparian areas of this study are similar, we expect similar temperature differences to occur when the satellite passes over around 10:30 am. The incoming short and longwave radiation are equal for the bare soil and the vegetation; therefore, the net radiation will depend on the outgoing short and long wave radiation. The albedo and surface temperature of dry bare soils during the day are higher than of vegetation resulting in more reflection of short wave radiation and more emission of long wave radiation which results in a lower R_n through the day for bare soil. During the night the surface temperatures of vegetation and bare soil are similar. However, due to the higher emissivity of vegetation (0.99) as compared to bare soil (0.94) (Humes et al., 1994), the R_n of vegetation is lower. (Hong, 2008) calculated that the daily R_n difference between vegetation and soil will be considerably smaller than the instantaneous R_n difference around 10:30 am.

Differences between vegetation and soil have been quantified by comparing the RS-estimated instantaneous and daily net radiation for fully vegetated agricultural fields, saltcedar, and bare soils (Table 5). Whereas the measured instantaneous net radiation fluxes of fully cropped agricultural fields and saltcedar stands exceeded those of bare soils by 54 to 77 %, the daily net radiation fluxes were only 20 to 36 % larger. A typical leaf area index (LAI) for saltcedar in the Middle Rio Grande Valley is about 2.5 (Cleverly et al., 2002) which indicates that bare soil is present but vegetation cover is dominant. Assume a typical mixed pixel with a soil cover of 75% saltcedar and 25% bare soil. The data from Table 5 for the first saltcedar plot show that the ratios between 100% saltcedar and 100% bare soil for instantaneous and daily R_n are 1.77 and 1.34. We want to estimate ratios between 100% saltcedar and a hypothetical mixed pixel. Using the values in Table 5 for the instantaneous and daily R_n for saltcedar and bare soil, and ignoring the effect of thermal radiation from soil that is intercepted by adjacent vegetation, the instantaneous and daily R_n for the mixed pixel are $0.75 \times 670 + 0.25 \times 379 = 598$ Wm^{-2} and $0.75 \times 19.8 + 0.25 \times 14.8 = 14.9 + 3.7 = 18.6$ MJm^{-2}day^{-1}. The net instantaneous and daily R_n of a fully vegetated saltcedar pixel are 670/598 = 1.12 and 19.8/18.6 = 1.06 times those of the hypothetical mixed pixel. The 12% difference is similar to the MRD's of 13 – 15% for the difference in instantaneous R_n between ground measurements and RS-based estimates (Table 4). The 6% difference for daily R_n falls within error ranges of radiation measurements (Halldin and Lundroth, 1992;Field et al., 1992). Thus, the much smaller MRD for daily R_n (-2.3 to -2.9 %) compared to the MRD of instantaneous R_n (about 13 %) can be explained by environmental radiation physics and is not an artefact of bias in the RS method or in the ground-based radiation sensors. This corroborates our interpretation that the RS-estimated net radiation for the 900 m^2 of the EC tower pixel is more representative for each site than the ground measurements with the net radiation meter preferentially positioned over a 10 m^2 patch of vegetation.

4.3. Comparison of RS-estimated Soil Heat Flux with Ground Measurements

The magnitude of soil heat flux, *G*, depends on surface cover, soil water content, and solar irradiance. For a moist soil beneath a plant canopy or residue layer, the instantaneous *G* will often be less than ±20 Wm^{-2} (Sauer, 2002b) while a bare, dry, exposed soil in midsummer could have a day-peak in excess of 300 Wm^{-2} (Fuchs and Hadas, 1973). In the Middle Rio Grande Basin during summer typical midday (10 am through 2 pm) values of *G* averaged 104 and 132 Wm^{-2} for upland grassland and shrubs, respectively (Kurc and Small, 2004). Instantaneous *G* in riparian areas is an important component of the energy balance that needs to be taken into account.

For this study six soil heat flux measurements were available from the Owens Valley and the San Pedro Valley data set. The RS-determined *G* approximates the ground measured *G* reasonably well (Figure 7) but the MRD is relatively high with values of 30.9 to 32.2 % (Table 6). However, the overall impact of the relatively high MRD in instantaneous *G* is relatively small since the MAD (35 W/m^2, Table 6) is only 6 % of the RS-predicted instantaneous net radiation and 5% of the ground measured instantaneous R_n. The daily *G* is near zero since heat enters the soil during the day but leaves the soil during the night (Table 6).

Given the high spatial and temporal variability of *G* (Sauer, 2002b) at the scale of a Landsat pixel, the reasonable agreement between RS-predicted instantaneous *G* and ground measurements, the relatively minor impact of an error in *G* on the estimates of *ET*, and the impracticality of measuring a truly representative *G* for a 900 m^2 heterogeneous pixel, it appears that assuming *G* is negligible within SEBAL and METRIC is acceptable.

4.4. Comparison of RS-based Sensible and Latent Heat Fluxes with Ground Measurements

Our data set covers a wide range of conditions varying from dry to moist which allows evaluation of SEBAL over a wide range of environmental conditions in riparian areas. Plots of instantaneous and daily SEBAL heat flux estimates versus ground measurements are presented in Figure 8. The ground measured instantaneous and daily *H* have two and six negative data points indicating regional advection. Advection is relatively minor for the instantaneous fluxes during satellite overpass time of around 10:30 am but increases considerably during late morning and early afternoon. The SEBAL estimated instantaneous and daily *H* that correspond with negative values of the ground measurements are near zero since the surface temperatures of the pixels are similar to the cold pixel temperature. When high quality hourly meteorological data are available regional advection can be accounted for in SEBAL by defining an advection enhancement parameter that is a function of soil moisture and weather conditions (Bastiaanssen et al., 2006;Allen et al., 2011) or one could implement METRIC (Allen et al., 2007), which has an implicit handling of advection due to its use of Penman-Monteith-based reference ET. However, in this study our aim is to evaluate the performance of the original SEBAL in heterogeneous arid environments where no weather data are used. The data in Figure 8 show that ignoring regional advection results in a maximum underestimation of the instantaneous and daily *LE* by, respectively, about 10 and 20% under moist conditions and when C_{EF} = 1.0; it becomes considerably less when the soil dries out. In this study we have removed all data related to negative instantaneous and daily *H* so that advection effects will not interfere with our evaluation of the original SEBAL approach (Allen et al., 2011;Bastiaanssen et al., 1998a).

4.4.1. Comparison of instantaneous heat fluxes

Figures 9 and 10 present plots of the adjusted *H* and *LE* measured at the EC tower versus the SEBAL estimates for scenarios S1 through S5. There was a substantial mismatch between the SEBAL estimated instantaneous *H* and the ground measurements (S1–S3), but if the SEBAL R_n is used in the ground measured energy balance, the correspondence was much improved (e.g. scenarios S4 and S5 in Figure 9). This is due to the bias-correction strategy of SEBAL and METRIC where biases in R_n and *G* are incorporated into estimates for *H*. SEBAL estimated instantaneous *LE* and ground measurements show good agreement for all five scenarios (S1 – S5) including the ones with a poor sensible heat flux match (Figure 10, S1-S3). The prediction of *LE* is good for scenarios S1–S5 with a mean MRD of -5.1% (Table 7) which is less than the average 14% deviation reported for SEBAL applications worldwide (Bastiaanssen et al., 2005).

The ground measured instantaneous *H* and *LE* presented in Table 7 are identical in S1–S3 but differ slightly from each other in S4 and S5 due to a slight difference in the temperature of the cold pixels that were chosen to estimate air temperature for calculation of the incoming long wave radiation. As a result the instantaneous net radiation used in scenarios S4 and S5 were also slightly different. However, a large difference existed between the ground measured *H* and *LE* in S1–S3 versus those in S4–S5 caused by the bias in instantaneous R_n of the ground measurements versus R_n determined with SEBAL (Table 4). In Table 7 the *H* and *LE* from SEBAL for the EM approaches (S3 and S5) are identical because EC measured instantaneous *LE* was not used for calibration; one set of cold and hot pixels are used for both scenarios. However, for S1, S2 and S4 a different set of cold and hot pixels were chosen for each scenario by forcing the constants c_1 and c_2 in Eq. [4] to fit the instantaneous *LE* measurements at the EC towers. This produced quite different *H* and *LE* SEBAL estimates for S1, S2 and S4.

In scenarios S1 and S2 of Table 7 there is no significant difference between the SEBAL estimated *H* (156 versus 138 W/m^2) and *LE* (314 versus 333 W/m^2). SEBAL calibrations based on the instantaneous *LE* of the tower pixels (S2) or on the *LE* of the instantaneous foot prints during the satellite's overpass (S1) yielded similar results except that the MAD and RMSD of S1 were lower (MAD/RMSD values for S1 and S2 were 39/57 and 56/74, respectively). This finding is relevant for practitioners who need to calibrate SEBAL on a routine basis and/or in nearly real-time. Using only the tower pixel is much faster and easier to implement automatically than determination of a weighted average within the tower footprint. However, for *posterior* SEBAL analyses and research applications use of the footprint is still recommended because (1) it has a better correspondence with ground measurements (Table 7) and (2) footprint analyses are effective for the detection of unusual environmental conditions.

The MAD and RMSD of *H* for S1, S2 and S3 are quite similar but rather high with MAD/RMSD values of 108/131, 126/147 and 111/135, respectively. The values of S4 and S5 (36/46 and 61/77) are considerably lower reflecting the ground energy balance correction by relying on the RS-based R_n. The MAD/RMSD values of the *LE* range from values of 39/57 for S1, 56/74 for S2, and 66/81 for S3. Values for S4 and S5 (39/48 and 61/77) were similar to S1, S2, and S3. Using the RS-based R_n had a much smaller effect on *LE* estimates than the *H* estimates which is a consequence of the internal calibration of SEBAL and METRIC.

MRD values exhibited the same trends observed in the MAD and RMSD values (Table 7). A striking feature in S1–S3 is the very poor prediction of *H*: with MRD's were between 35 and 47 %. This result was not expected, especially, for S1 and S2 that were calibrated against ground measured instantaneous *LE*. The discrepancy was the result of the apparent bias in the ground measurements of R_n discussed previously (see Section [4.2]). Substituting the RS-based R_n for the ground measured R_n improved the RS-based estimates of *H* dramatically: MRD's of S4 and S5 were 0.8 and 16.6 %, respectively. Despite the poor MRD's of *H* (35 to 47 %), in S1 – S3, the SEBAL *LE* estimates exhibited good MRD's (2.7 to -11.5 %). Although RS-based estimates of *H* had high error, the internal calibration procedure protects against inaccurate estimates of *LE*.

Calibrating SEBAL with reliable ground measurements at the pixel scale improved estimates of both *H* and *LE*. However, ground measurements of *H* should be used cautiously and carefully for the calibration and evaluation of SEBAL because the RS-based *H* estimate compensates for error in R_n, *G*, and aerodynamics, and can deviate from the ground-based measurements. Lumping error into *H* is a necessary characteristic of SEBAL and METRIC designed to arrive at unbiased estimates for *LE*.

The internal calibration of *H* and *LE* using cold and hot pixels in SEBAL and METRIC reduces or cancels bias introduced by the calculation of albedo, net radiation, and surface temperature as well as errors in narrow band emissivity, atmospheric correction, satellite sensor, aerodynamic resistance, and soil heat flux. This procedure can result in a reduction of total bias in ET of as much as 30 % compared to other models that are not routinely internally calibrated (Allen et al., 2006). Allen et al. (2007) describe how METRIC, through the use of weather based reference ET, is able to eliminate most internal energy balance component biases at both the cold and hot extreme conditions. SEBAL, on the other hand, eliminates bias at the hot extreme, but necessarily retains a bias at the cold extreme where it is assumed that $LE = R_n - G$. The cost for the improved estimates for LE is a deterioration of the SEBAL and METRIC H estimates since H, as an intermediate parameter, absorbs most of the aforementioned bias as a result of the internal calibration process (Choi et al., 2009).

4.4.2. Comparison of daily sensible and latent heat fluxes

The ground measured daily evaporative fraction (EF_{24}) is larger than the instantaneous evaporative fraction (EF_{inst}) (Figure 11). A simple linear regression yielded a small not significant intercept of 0.04 (p>0.05) and a slope of 1.19 (95 % confidence interval 0.99 to 1.36). The traditional SEBAL application assumes c_{EF} = 1.0 (Bastiaanssen et al., 1998a), but several field studies suggest the value is closer to 1.1 (Brutsaert and Sugita, 1992;Anderson et al., 1997). While recognizing that 1.19 is closer to 1.1 than to 1.0, we examined the effects of both estimates for c_{EF} on the conversion from instantaneous LE to daily LE (see Eq. [5]).

Figures 12 and 13 present the plots of the adjusted (using ground measured R_n energy balance closure) H and LE daily heat fluxes measured at the EC towers versus the SEBAL estimates resulting from scenarios S1–S3 with c_{EF} set to 1.1. Scenarios S4 and S5 are not shown because the daily R_n measured on the ground and determined by SEBAL were similar (Table 4). For the values in Table 8, when the c_{EF} = 1.0, the agreement was excellent for the daily LE (mean MRD of 3.9% = [2.9+0.0+8.9]/3) but was rather poor for the H (mean MRD of -20.4% = [-19.4-14.9-27.0]/3). Next, using a c_{EF} value of 1.1, SEBAL estimated LE increased, therefore MRDs (MRD = $(\overline{G} - \overline{S})/\overline{G}$) of LE decreased to be negative so that MRDs of H improved (less negative). As a result, the assumption c_{EF} = 1.1 leads to a better agreement for H (Table 8).

Although our results do not suggest with certainty which of the c_{EF} values yields more accurate estimates of *H* and *LE* we recommend the use of 1.1 based on our study (Figure 11), results reported in the literature (Brutsaert and Sugita, 1992;Anderson et al., 1997), and the improved daily *H* fluxes from SEBAL (Table 8).

A comparison between ground measurements and SEBAL estimates of daily evapotranspiration is shown in Figure 14. Linear relationships between unadjusted EC measurements of *ET* and SEBAL estimates of *ET* based on c_{EF} = 1.1 are evident. For scenarios S1, S2, and S3 the slopes of the relationship varied between 1.32 and 1.08 (mean of 1.23) suggesting that SEBAL *ET* estimates were about 21% higher than the unadjusted *ET* measurements at the EC towers. This discrepancy is consistent with other studies that reported systematic underestimation of heat fluxes by the eddy covariance method can be as high as 10 to 30 % (Twine et al., 2000;Paw et al., 2004). Given the inherent uncertainties of the SEBAL approach and the eddy covariance method the linear relationships between the two methods are surprisingly good. The SEBAL/METRIC approach is a powerful tool for high resolution mapping of evapotranspiration even where no meteorological measurements are available on the ground. This study also demonstrates that the use of SEBAL or METRIC in heterogeneous landscapes such as arid riparian areas results in *ET* estimates that are as good as those that could be obtained using the EC method.

5. CONCLUSIONS

We have evaluated the SEBAL extreme-condition-inverse calibration remote sensing model in arid riparian areas by comparing instantaneous and daily energy balance components with those measured on the ground with the eddy covariance method.

An analysis of differences in instantaneous R_n during late morning between vegetation and exposed soil emphasizes the importance of selecting representative soil and vegetative mixture viewed by the ground R_n sensor. We argue that tower-based R_n is generally biased toward vegetation, resulting in exaggerated R_n values within the eddy covariance footprint. Instantaneous R_n from RS, representing a larger area than the net radiometer, systematically gave lower instantaneous R_n values. When these were used to close the eddy covariance energy balance, *LE* and *H* from SEBAL and ground based eddy covariance were more similar. Daily R_n values of SEBAL agreed well with the ground measurements. This result can be ascribed to physical differences between the radiation balance of pixels of mixed riparian vegetation and bare soil compared to the small footprint of ground R_n sensors placed over vegetation

Instantaneous *G* values of SEBAL were about 30% higher than the ground measured values in the San Pedro and Owens Valley. However, this large relative difference had a relatively minor impact on the overall energy balance because the actual deviation in *G* was approximately 5-6 % of the SEBAL and ground measured instantaneous R_n. Also, daily *G* is near zero because heat enters the soil during the day and exits the soil during the night. In the application of SEBAL and METRIC for estimating daily *ET*, it is reasonable to assume *G* is negligible.

Instantaneous *LE* values derived from SEBAL were within -13.2 to 2.7% of the ground measurements for five different comparisons (scenarios S1-S5). The magnitude of these differences was similar to the variability common to eddy covariance flux measurements, i.e. it was not possible in this study of heterogeneous arid riparian areas to determine conclusively whether the difference between methods was a result of bias in SEBAL or the eddy covariance method.

Instantaneous *H* values of SEBAL differed from the ground measurements by 35.0 to 47.2%. These *H* fluxes are necessarily biased because errors in R_n and *G* are lumped into *H* as a result of the extreme-condition-inverse internal calibration procedure. Substitution of the ground measured R_n for the SEBAL R_n in the ground based energy balance improved the comparison with the RS-based *H* with relative differences of only 0.8% and 16.6%. Using a combination of ground measured *G* and *H* with RS-based R_n yielded the least biased energy balances over heterogeneous arid riparian areas.

Daily *H* and *LE* fluxes estimated by SEBAL generally agreed with ground measurements (mean MRD'S 13.8 to -0.7%). Better agreement at the daily scale was largely due to the better correspondence in daily rather than instantaneous R_n estimates between SEBAL and ground measurements. The use of a multiplier on the instantaneous evaporative fraction of 1.1 to convert the instantaneous ET to daily ET was preferable for the non-advective conditions during the months April to September.

The instantaneous SEBAL *H* is intentionally biased during calibration and expected to deviate from the ground measured *H* in order to provide an unbiased estimate of *LE* For all five calibration scenarios, the comparison measures (r^2, MAD, RMSD and MRD) of the instantaneous and daily *LE* fluxes were strong evidence that the great strength of the SEBAL and METRIC method is their internal calibration procedure that eliminates most of the error in *LE* flux at the expense of increased error in instantaneous *H* flux. We conclude that the SEBAL method is an effective tool for mapping actual evapotranspiration at high spatial resolution in heterogeneous riparian areas where hourly weather data are unavailable.

ACKNOWLEDGEMENT

The following sponsors have contributed to this study: NSF EPSCoR grant EPS-0447691; U.S. Department of Agriculture, CSREES grant No.: 2003-35102-13654; New Mexico Universities Collaborative Research (NUCOR) program for joint research with the Los Alamos National Laboratory; and NASA New Investigator Program. The energy balance data from towers in the Middle Rio Grande Valley were provided by Dr. James Cleverly of the University of New Mexico. We did our own energy balance adjustment.

REFERENCES

Allen, R. G., Pereira, L. S., Raes, D., and Smith, M.: Crop evapotranspiration, FAO Irrigation and drainage paper 56, FAO. Rome, 1998.

Allen, R. G., Tasumi, M., and Trezza, R.: M E T R I C^{tm} Mapping Evapotranspiration at High Resolution. Applications Manual for Landsat Satellite Imagery. Version 2.0, University of Idaho, Kimberly, Idaho, 139, 2005.

Allen, R. G., Tasumi, M., and Trezza, R.: Benefits from tying satellite-based energy balance to reference evapotranspiration, Earth Observation for Vegetation Monitoring and Water Management. AIP Conference Proceedings, 852, 127-137, 2006.

Allen, R. G., Tasumi, M., and Trezza, R.: Satellite-based Energy Balance for Mapping Evapotranspiration with Internalized Calibration (METRIC) – Model, Journal of Irrigation and Drainage Engineering, 133, 380-394, 2007.

Allen, R. G., Irmak, A., Trezza, R., Hendrickx, J. M. H., Bastiaanssen, W. G. M., and Kjaersgaard, J.: Satellite-based ET estimation in agriculture using SEBAL and METRIC, Hydrologic Processes, 25, 4011-4027, 2011.

Anderson, M. C., Norman, J. M., Diak, G. R., Kustas, W. P., and Mecikalski., J. R.: A two-source time-integrated model for estimating surface fluxes using thermal infrared remote sensing, Remote Sensing of Environment, 60, 195-216, 1997.

Arya, P. S.: Introduction to micrometeorology, Academic press, 2001.

Bastiaanssen, W. G. M.: Regionalization of surface flux desities and moisture indicators in composite terrain: a remote sensing approach under clear skies in Mediterranean climates, Landbouwuniversiteit te Wageningen, 1995.

Bastiaanssen, W. G. M., Menenti, M., Feddes, R. A., and Holtslag, A. A. M.: A remote sensing surface energy balance algorithm for land (SEBAL). Part 1: Formulation, Journal of Hydrology, 212-213, 198-212, 1998a.

Bastiaanssen, W. G. M., Pelgrum, H., Wang, J., Ma, Y., Moreno, J. F., Roerink, G. J., Roebeling, R. A., and Wal, T. v. d.: A remote sensing surface energy balance algorithm for land (SEBAL). Part 2: Validation, Journal of Hydrology, 212-213, 213-229, 1998b.

Bastiaanssen, W. G. M.: SEBAL-based sensible and latent heat fluxes in the Irrigated Gediz Basin, Turkey, Journal of Hydrology, 229, 87-100, 2000.

Bastiaanssen, W. G. M., Ahmad, M.-D., and Chemin, Y.: Satellite surveillance of evaporative depletion across the Indus Basin, Water Resources Research, 38, 1273, doi:1210.1029/2001WR000386, 2002.

Bastiaanssen, W. G. M., Noordman, E. J. M., Pelgrum, H., Davids, G., Thoreson, B. P., and Allen, R. G.: SEBAL model with remotely sensed data to improve water-resources management under actual field conditions, Journal of Irrigation and Drainage Engineering, 131, 85-93, 2005.

Bastiaanssen, W. G. M., Klaasse, A., Zwart, S., Immerzeel, W., and Droogers, P.: The hydrological flow path and options for sustainable water resources management in the overexploited Rio Bravo Basin, A world bank project, Final report, 102p, 2006.

Brutsaert, W., and Sugita, M.: Application of self-preservation in the diurnal evolution of the surface energy budget to determine daily evaporation, Journal of Geophysical Research, 97, 18,377-318,382, 1992.

Brutsaert, W., Hsu, A. Y., and Schmugge, T. J.: Parameterization of surface heat fluxes above a forest with satellite thermal sensing and boundary layer soundings, Journal of Applied Meteorology, 32, 909-917, 1993.

Choi, M., Kustas, W. P., Anderson, M. C., Allen, R. G., Li, F., and Kjaersgaard, J. H.: An intercomparison of three remote sensing-based surface energy balance algorithms over a corn and soybean production region (Iowa, US) during SMACEX, Agricultural and Forest Meteorology, 149, 2082-2097, 2009.

Choudhury, B. J.: Estimating evaporation and carbon assimilation using infrared temperature data: vistas in modeling, Theory and Application of Remote Sensing, edited by: Asrar, G., Wiley, New York, 628-690 pp., 1989.

Cleverly, J. R., Dahm, C. N., Thibault, J. R., Gilroy, D. J., and Coonrod, J. E. A.: Seasonal estimates of actual evapo-transpiration from Tamarix ramosissima stands using three-dimensional eddy covariance, Journal of Arid Environments, 52, 181-197 doi:110.1006/jare.2002.0972, 2002.

Compaoré, H., Hendrickx, J. M. H., Hong, S.-h., Friesen, J., van de Giesen, N. C., Rodgers, C., Szarzynski, J., and Vlek, P. L. G.: Evaporation mapping at two scales using optical imagery in the White Volta Basin, Upper East Ghana Physics and Chemistry of the Earth, Parts A/B/C, 33, 127-140, doi:110.1016/j.pce.2007.1004.1021, 2008.

Costigan, K. R., Bossert, J. E., and Langley, D. L.: Atmospheric/hydrologic models for the Rio Grande Basin: simulations of precipitation variability, Global and Planetary Change, 25, 83-110, 2000.

Crago, R. D.: Conservation and variability of the evaporative fraction during the daytime, Journal of Hydrology, 180, 173-194, 1996.

De Bruin, H. A. R.: In: J.C Hooghart (Ed.), From Penman to Makkink, Evaporation and weather. Proceedings and Information No. 39, TNO Committee on Hydrological Research, The Hague, pp. 5-31., 1987.

De Bruin, H. A. R., Bink, N. J., and Kroon, L. J. M.: Fluxes in the surface layer under advective conditions, Land surface evaporation, edited by: Schmugge, T. J., and Andre, J.-C., Springer-Verlag New York, Inc., 1991.

Droogers, P., and Allen, R. G.: Estimating reference evapotranspiration under inaccurate data conditions, Irrigation and Drainage Systems, 16, 33–45, 2002.

Du, J., Song, K., Wang, Z., Zhang, B., and Liu, D.: Evapotranspiration Estimation Based on MODIS Products and Surface Energy Balance Algorithms for Land (SEBAL) Model in Sanjiang Plain, Northeast China., Chinese Geographical Science, 23, 73-91, 2013.

Elmore, A. J., Mustard, J. F., and Manning, S. J.: Regional patterns of plant community response to changes in water: Owens Valley, California., Ecological Applications, 13, 443-460, 2002.

Farah, H. O., Bastiaanssen, W. G. M., and Feddes, R. A.: Evaluation of the temporal variability of the evaporative fraction in a tropical watershed, International Journal of Applied Earth Observation and Geoinformation 5, 129-140, 2004.

Field, R. T., Fritschen, L. J., Kanemasu, E. T., Smith, E. A., Stewart, J. B., Verma, S. B., and Kustas, W. B.: Calibration, comparison and correction of net radiation instruments used during FIFE, Journal of Geophysical Research, 97, 18681-18695, 1992.

Fox, D. G.: Judging air quality model performance: A summary of the AMS Workshop on Dispersion Model Performance, Bulletin of the American Meteorological Society, 62, 599-609, 1981.

Franks, S. W., and Beven, K. J.: Estimation of evapotranspiration at the landscape scale: a fuzzy disaggregation approach, Water Resources Research, 33, 2929-2938, 1997.

Fuchs, M., and Hadas, A.: Analysis and performance of an improved soil heat flux transducer, Soil Science Society of America, Proceedings, 37, 173-175, 1973.

Gibson, L. A., Jarmain, C., Su, Z., and Eckardt, F.: Review: Estimating evapotranspiration using remote sensing and the Surface Energy Balance System – A South African perspective, Water SA, 39, 477-483, 2013.

Granger, R. J.: Satellite-derived estimates of evapotranspiration in the Gediz basin, Journal of Hydrology, 229, 70-76, 2000.

Halldin, S., and Lundroth, A.: Errors in net radiometry: comparison and evaluation of six radiometer designs, ournal

of Atmospheric and Oceanic Technology, J6, 762-783, 1992.
Hemakumara, H., Chandrapala, L., and Moene, A.: Evapotranspiration fluxes over mixed vegetation areas measured from a large aperture scintillometer, Agricultural Water Management, 58, 109–122, 2003.
Hendrickx, J. M. H., Vink, N. H., and Fayinke, T.: Water requirement for irrigated rice in a semi-arid region in West Africa, Agricultural Water Management, 11, 75-90, 1986.
Hong, S.-H.: Mapping regional distributions of energy balance components using optical remotely sensed imagery. Ph.D. Dissertation Thesis, New Mexico Institute of Mining and Technology, Socorro NM, 378 pp., 2008.
Hsieh, C.-I., Katul, G. G., and Chi, T.-W.: An approximate analytical model for footprint estimation of scalar fluxes in thermally stratified atmospheric flows, Advances in Water Resources, 23, 765-772, 2000.
Humes, K. S., Kustas, W. P., Moran, M. S., Nichols, W. D., and Weltz, M. A.: Variability of emissivity and surface temperature over a sparsely vegetated surface, Water Resources Research, 30, 1299-1310, 1994.
Jacob, F., Olioso, A., Gu, X. F., Su, Z., and Seguin, B.: Mapping surface fluxes using airborne visible, near infrared, thermal infrared remote sensing data and a spatialized surface energy balance model, Agronomie, 22, 669–680 669 DOI: 610.1051/agro:2002053, 2002.
Jiang, L., and Islam, S.: Estimation of surface evaporation map over southern Great Plains using remote sensing data, Water Resources Research, 37, 329-340, 2001.
Karimi, P., and Bastiaanssen, W. G. M.: Spatial evapotranspiration, rainfall and land use data in water accounting – Part 1: Review of the accuracy of the remote sensing data, Hydrol. Earth Syst. Sci., 19, 507-532, 2015.
Kite, G. W., and Droogers, P.: Comparing evapotranspiration estimates from satellites, hydological models and field data, Journal of Hydrology, 229, 3-18, 2000.
Kizer, M. A., and Elliott, R. L.: Eddy correlation systems for measuring evapotranspiration, Transactions of American Society of Agricultural Engineers, 34, 387-392, 1991.
Kleissl, J., Gomez, J. D., Hong, S.-H., and Hendrickx, J. M. H.: Large aperture scintillometer intercomparison study, Boundary-Layer Meteorology, 128, 133-150, 2008.
Kleissl, J., Hong, S.-H., and Hendrickx, J. M. H.: New Mexico scintillometer network. Supporting remote sensing and hydrologic and meteorological models, Bulletin American Meteorological Society, 90, 207-218, 2009.
Kurc, S. A., and Small, E. E.: Dynamics of evapotranspiration in semiarid grassland and shrubland ecosystems during the summer monsoon season, central New Mexico, Water Resources Research, 40, W09305, doi:09310.01029/02004WR003068, 2004.
Kustas, W. P., and Norman, J. M.: Use of remote sensing for evapotranspiration monitoring over land surfaces, Hydrological Sciences Journal, 41, 495-516, 1996.
Kustas, W. P., Prueger, J. H., Hatfield, J. L., Ramalingam, K., and Hipps, L. E.: Variability in soil heat flux from a mesquite dune site, Agricultural and Forest Meteorology, 103, 249– 264, 2000.
Loescher, H. W., Ocheltree, T., Tanner, B., Swiatek, E., Dano, B., Wong, J., Zimmerman, G., Campbell, J., Stock, C., Jacobsen, L., Shiga, Y., Kollas, J., Liburdy, J., and Law, B. E.: Comparison of temperature and wind statistics in contrasting environments among different sonic anemometer-thermometers, Agricultural Forest Meteorol., 133, 119-139, 2005.
Ma, Y., Menenti, M., Tsukamoto, O., Ishikawa, H., Wang, J., and Gao., Q.: Remote sensing parameterization of regional land surface heat fluxes over arid area in northwestern China, Journal of Arid Environments, 57, 257-273, 2004.
Moran, M. S., and Jackson, R. B.: Assessing the spatial distribution of evapotranspiration using remotely sensed inputs, Journal of Environmental Quality, 20, 725-735, 1991.
Mu, Q., Zhao, M., and Running, S. W.: Improvements to a MODIS global terrestrial evapotranspiration algorithm, Remote Sensing of Environment, 115, 1781-1800, 2011.
Norman, J. M., Kustas, W. P., and Humes, K. S.: A two-source approach for estimating soil and vegetation energy fluxes from observations of directional radiometric surface temperature, Agriculture and Forest Meteorology, 77, 263-293, 1995.
Norman, J. M., Anderson, M. C., Kustas, W. P., French, A. N., Mecikalski, J., Torn, R., Diak, G. R., Schmugge, T. J., and Tanner, B. C. W.: Remote sensing of surface energy fluxes at 10 1-m pixel resolutions, Water Resources Research, 39, 1221. doi:1210.1029/2002WR001775., 2003.
Parlange, M. B., Eichinger, W. E., and Albertson, J. D.: Regional scale evaporation and the atmosphere boundary layer, Reviews of Geophysics, 33, 99-124, 1995.
Paw, K. T., Wharton, S., Xu, L., Falk, M., Schroeder, M., and Gonzales, E.: Zen and the art of energy balance

closure, Symposium “Progress in Radiation and Energy Balance Closure”, 68th Annual Meeting Soil Science Society of America, Seattle, Washington, 2004.

Pelgrum, H., and Bastiaanssen, W. G. M.: An intercomparison of techniques to determine the area-averaged latent heat flux from individual in situ observations: a remote sensing approach using the European Field Experiment in a Desertification-Threatened Area data, Water Resources Research, 32, 2775–2786, 1996.

Sauer, T. J.: Soil Heat Flux. Encyclopedia of Soil Science, edited by: Lal, R., Marcel Dekker, INC., New York, NY, 647-649 pp., 2002a.

Sauer, T. J.: Heat flux density, in: Methods of soil analysis. Part 1, edited by: Dane, J., and Topp, C., Soil Science Society of America Madison, Wisconsin, 1233-1248, 2002b.

Sauer, T. J., Meek, D. W., Ochsner, T. E., Harris, A. R., and Horton, R.: Errors in heat flux measurement by flux plates of contrasting design and thermal conductivity, Vadose Zone Journal, 2, 580-588, 2003.

Schmid, H. P., and Oke, T. R.: A model to estimation the source area contributing to turbulent exchange in the surface layer over patchy terrain, Quarterly Journal of The Royal Meteorological Society, 116, 965-988, 1990.

Schuepp, P. H., Leclerc, M. Y., MacPherson, J. I., and Desjardins, R. L.: Footprint prediction of scalar fluxes from analytical solutions of the diffusion equation, Boundary-Layer Meteorology, 50, 355-373, 1990.

Schüttemeyer, D., Schillings, C., Moene, A. F., and Bruin, H. A. R. D.: Satellite-based actual evapotranspiration over drying semiarid terrain in West Africa, Journal of Applied Meteorology and Climatology, 46, 97-111 DOI: 110.1175/JAM2444.1171, 2007.

Scott, R. L., Shuttleworth, J. W., Goodrich, D. C., and Maddock III, T.: The water use of two dominant vegetation communities in a semiarid riparian ecosystem, Agricultural and Forest Meteorology, 105, 241-256, 2000.

Scott, R. L., Edwards, E. A., Shuttleworth, W. J., Huxman, T. E., Watts, C., and Goodrich, D. C.: Interannual and seasonal variation in fluxes of water and carbon dioxide from a riparian woodland ecosystem, Agricultural and Forest Meteorology, 122, 65–84, 2004.

Seguin, B. D., and Itier, B.: Using midday surface temperature to estimate daily evapotranspiration from satellite thermal IR data, International Journal of Remote Sensing, 4, 371-383, 1983.

Senay, G. B., Bohms, S., Singh, R. K., Gowda, P. H., Velpuri, N. M., Alemu, H., and Verdin, J. P.: Operational evapotranspiration mapping using remote sensing and weather datasets: A new parameterization for the SSEB approach, JAWRA Journal of the American Water Resources Association, 49, 577-591, 2013.

Steinwand, A. L., Harrington, R. F., and Or, D., 2006.: Water balance for Great Basin phreatophytes derived from eddy covariance, soil water, and water table measurements, Journal of Hydrology, 329, 595-605, 2006.

Stromberg, J. C.: Dynamics of Fremont cottonwood (Populus fremontii) and saltcedar (Tamarix chinensis) populations along the San Pedro River, Arizona, Journal of Arid Environments, 40, 133-155, 1998.

Su, Z.: The Surface Energy Balance System (SEBS) for estimation of turbulent heat fluxes, Hydrology and Earth System Sciences, 6, 85-99, 2002.

Sugita, M., and Brutsaert, W.: Daily evaporation over a region from lower boundary layer profiles measured with radiosondes, Water Resources Research, 27, 747-752, 1991.

Tasumi, M.: Progress in operational estimation of regional evapotranspiration using satellite imagery, Ph.D. Thesis, University of Idaho, Moscow, Idaho, 2003.

Teixeira, A. H. d. C., Bastiaanssen, W. G. M., Moura, M. S. B., Soares, J. M., Ahmad, M. D., and Bos, M. G.: Energy and water balance measurements for water productivity analysis in irrigated mango trees, Northeast Brazil, Agricultural and Forest Meteorology, 148, 1524-1537, 2008.

Trezza, R.: Evapotranspiration using a satellite-based surface energy balance with standardized ground control. Ph.D. Thesis, Utah State University: Logan, Utah., 2002.

Twine, T. E., Kustas, W. P., Norman, J. M., Cook, D. R., Houser, P. R., Meyers, T. P., Prueger, J. H., Starks, P. J., and Wesely, M. L.: Correcting eddy-covariance flux underestimates over a grassland, Agricultural and Forest Meteorology, 103, 279-300, 2000.

Wang, J., Bastiaanssen, W. G. M., Ma, Y., and Pelgrum, H.: Aggregation of land surface parameters in the oasis-desert systems of Northwest China, Hydrological Sciences, 12, 2133-2147, 1998.

Willmott, C. J., and Wicks, D. E.: An empirical method for the spatial interpolation of monthly precipitation within California, Physical Geography, 1, 59-73, 1980.

Willmott, C. J.: On the validation of models, Physical Geography, 2, 184-194, 1981.

Willmott, C. J.: Some comments on the evaluation of model performance, Bulletin of the American Meteorological Society, 63, 1309–1313, 1982.

Wilson, K., Goldstein, A., Falge, E., Aubinet, M., Baldocchi, D., Berbigier, P., Bernhofer, C., Ceulemans, R., Dolman, H., Field, C., Grelle, A., Ibrom, A., Law, B. E., Kowalski, A., Meyers, T., Moncrieff, J., Monson, R., Oechel, W., Tenhunen, J., Valentini, R., and Verma, S.: Energy balance closure at FLUXNET sites, Agric. For. Meteorol., 113, 223-243, 2002.

Wright, J. L.: New evapotranspiration crop coefficients, Journal of Irrigation and Drainage Engineering, 108, 57-74, 1982.

Yang, Y. T., and Shang, S. H.: A hybrid dual source scheme and trapezoid framework based evapotranspiration model (HTEM) using satellite images: algorithm and model test, Journal of Geophysical Research, 118, 2284-2300, 2013.

Zwart, S. J., and Leclert, L. M. C.: A remote sensing-based irrigation performance assessment: a case study of the Office du Niger in Mali, Irrigation science, 28, 371-385, 2010.

Table 1. List of Landsat 7 ETM+ images used in this study (overpass around 10:30 am).

Area	Date	Path/Row
Rio Grande	04/07/2000	33/36
Rio Grande	07/28/2000	33/36
Rio Grande	09/14/2000	33/36
Rio Grande	09/30/2000	33/36
Rio Grande	05/09/2000	33/36
Rio Grande	06/04/2001	34/36
Rio Grande	05/06/2002	34/36
Rio Grande	05/31/2002	33/36
Rio Grande	05/31/2002	33/37
Rio Grande	06/16/2002	33/36
Rio Grande	08/19/2002	33/36
Owens Valley	07/10/2002	41/34
Owens Valley	08/11/2002	41/34
Owens Valley	09/12/2002	41/34
San Pedro	05/16/2003	35/38
San Pedro	08/12/2003	35/38

Table 2. Site characteristics and sensor heights on the eddy covariance towers.

Site	Longitude/ Latitude	Vegetation type	Elevation (m)	Vegetation height (m)	Sensor height (m)
Rio Grande – BDAS	106.88W/ 33.78 N	saltcedar	1370	6.2	8.2
Rio Grande – BLN	106.75W/ 34.59N	cottonwood	1460	25.1	27.2
Rio Grande – SEV	106.87W/ 34.27N	saltcedar	1430	4.9	6.5
Rio Grande – SHK	106.68W/ 34.96N	cottonwood	1500	23.7	26.3
Owens – FSL138	118.43W/ 37.41N	alkali meadow	1280	0.2	2.5
Owens – PLC018	118.35W/ 37.37N	rabbitbrush scrub	1250	0.5	2.5
Owens – PLC074	118.36W/ 37.32N	saltbush meadow	1240	1.0	2.5
Owens – PLC185	118.33W/ 37.27N	desert sink scrub	1220	0.5	2.5
Owens – BLK100	118.24W/ 36.90N	alkali meadow	1170	0.2	2.5
San Pedro – CM	110.18W/ 31.66N	mesquite	1190	7.0	14
San Pedro – LSS	110.14W/ 31.56N	sacaton	1230	1.0	3.5
San Pedro – LSM	110.13W/ 31.57N	mesquite	1240	3.5	6.5

Table 3. Scenarios of comparison between RS-based estimates and ground measurements of net radiation R_n, soil heat flux G, and sensible and latent heat fluxes H and LE.

ID	**Scenario**	**R_n Used for Energy Balance Closure**
S1	EC Approach (EC_FP)[1]	Ground Measured R_n
S2	EC Approach (EC_TP)[2]	Ground Measured R_n
S3	EM Approach[3]	Ground Measured R_n
S4	EC Approach (EC_TP/SR$_n$)[4]	RS Estimated R_n
S5	EM Approach (SR$_n$)[5]	RS Estimated R_n

[1]Hot pixel selected by matching the ground measured instantaneous *LE* (adjusted for closure error using the ground measured R_n) at satellite overpass with the footprint weighted averaged SEBAL *LE*. SEBAL *LE* compared against ground measured instantaneous *LE* (adjusted for closure error using the ground measured R_n) at satellite overpass.
[2]Hot pixel selected by matching the ground measured instantaneous *LE* (adjusted for closure error using the ground measured R_n) at satellite overpass with the SEBAL *LE* at the tower pixel. SEBAL *LE* compared against ground measured instantaneous *LE* (adjusted for closure error using the ground measured R_n) at satellite overpass.
[3]Hot pixel selected by the empirical approach without use of ground measurements. SEBAL *LE* is compared against ground measured instantaneous *LE* (adjusted for closure error using the ground measured R_n) at satellite overpass.
[4]Hot pixel selected by matching the ground measured instantaneous *LE* (adjusted for closure error using the ground measured R_n) at satellite overpass with the SEBAL *LE* at the tower pixel. SEBAL *LE* compared against ground measured instantaneous *LE* (adjusted for closure error using the SEBAL estimated R_n) at satellite overpass.
[5]Hot pixel selected by the empirical approach without use of ground measurements. SEBAL *LE* is compared against ground measured instantaneous *LE* (adjusted for closure error using the SEBAL estimated R_n) at satellite overpass.

Table 4. Quantitative measures for comparison of RS-based instantaneous and daily net radiation estimates ($\overline{S}$) versus ground measurements ($\overline{G}$) using the EC and Empirical Approaches for selection of hot and cold pixels.

Selection Cold and Hot Pixel	n	$\overline{G}$	$\overline{S}$ [4]	SD_G	SD_S	r^2	MAD	RMSD	MRD
Instantaneous R_n	(-)	(W/m^2)	(W/m^2)	(W/m^2)	(W/m^2)	(-)	(W/m^2)	(W/m^2)	%
S1 - EC Approach (FP[1])	25	654	569	86	90	0.56	88	105	13.0
S2 - EC Approach (TP[2])	25	654	571	86	89	0.56	87	103	12.8
S3 - Empirical Approach	25	654	559	86	88	0.56	97	113	14.6
Daily R_n	(-)	($MJ/m^2/d$)	($MJ/m^2/d$)	($MJ/m^2/d$)	($MJ/m^2/d$)	(-)	($MJ/m^2/d$)	($MJ/m^2/d$)	%
S1/S2 - EC Approach[3]	24	15.6	16.0	3.1	3.1	0.75	1.3	1.6	-2.9
S3 - Empirical Approach	24	15.6	15.9	3.1	3.0	0.69	1.3	1.8	-2.3

[1]Cold and hot pixels were selected by matching the instantaneous *LE* measured at the EC tower with the footprint weighted averaged SEBAL instantaneous *LE*. [2]Cold and hot pixels were selected by matching the instantaneous *LE* measured at the EC tower with the SEBAL instantaneous *LE* of the EC tower pixel. [3]The daily R_n does not depend on the selection of the cold and hot pixels; both EC Approaches yield the same values. [4]The SEBAL instantaneous R_n estimate ($\overline{S}$) was obtained by calculating the footprint weighted average for the instantaneous R_n; the daily R_n ($\overline{S}$) was obtained as the average SEBAL daily R_n of the 25 pixels around the EC tower.

Table 5. Selected instantaneous and daily net radiation fluxes and relevant parameters for adjacent clusters of vegetated and bare soil pixels on June 16, 2002.

Vegetation	Albedo (-)		NDVI[1] (-)		T-surface (degree K)		Instantaneous Net Radiation (W/m^2)			Daily Net Radiation ($MJ/(m^2\ d)$)			N[2]
	Veg	Bare	Veg	Bare	Veg	Bare	Veg	Bare	Ratio	Veg	Bare	Ratio	
Alfalfa	0.22	0.32	0.84	0.14	299	325	634	384	1.65	17.9	14.8	1.21	50
Alfalfa	0.21	0.31	0.80	0.24	301	322	627	408	1.54	18.1	15.1	1.20	20
saltcedar	0.16	0.32	0.65	0.14	302	326	670	379	1.77	19.8	14.8	1.34	50
saltcedar	0.14	0.31	0.49	0.24	308	322	657	408	1.61	20.6	15.1	1.36	20

[1]NDVI = Normalized Difference Vegetation Index, [2]N = number of pixels in each

Table 6. Quantitative measures for comparison of instantaneous and daily RS-based soil heat flux estimates ($\overline{S}$) versus ground measurements ($\overline{G}$) using the EC and Empirical Approaches for selection of hot and cold pixels.

Selection Cold and Hot Pixel	N[4]	$\overline{G}$	$\overline{S}$ [5]	SD_G	SD_S	r^2	MAD	RMSD	MRD
Instantaneous G	(-)	(W/m^2)	(W/m^2)	(W/m^2)	(W/m^2)	(-)	(W/m^2)	(W/m^2)	%
EC Approach (FP[1])	6	76	101	26	13	0.02	35	35	-32.2
EC Approach (TP[2])	6	76	101	26	13	0.02	35	35	-31.9
Empirical Approach	6	76	100	26	13	0.02	34	34	-30.9
Daily G	(-)	(MJ/m^2/d)	(MJ/m^2/d)	(MJ/m^2/d)	(MJ/m^2/d)	(-)	(MJ/m^2/d)	(MJ/m^2/d)	%
EC Approach[3]	24	0.5	0.0	0.4	0.0	-	0.5	0.6	>100
Empirical Approach	24	0.5	0.0	0.4	0.0	-	0.5	0.6	>100

[1] Cold and hot pixels were selected by matching the instantaneous *LE* measured at the EC tower with the footprint weighted averaged SEBAL instantaneous *LE*. [2] Cold and hot pixels were selected by matching the instantaneous *LE* measured at the EC tower with the SEBAL instantaneous *LE* of the EC tower pixel. [3] The daily soil heat flux does not depend on the selection of the cold and hot pixels; both EC Approaches yield the same values. [4] No instantaneous soil heat flux measurements were available in the Middle Rio Grande Basin.[5] The RS-based instantaneous soil heat flux estimate ($\overline{S}$) was obtained by calculating the footprint average for the instantaneous soil heat flux; the daily soil heat flux ($\overline{S}$) was obtained as the average SEBAL daily soil heat flux of the 25 pixels around the EC tow.

Table 7. Quantitative measures for comparison of SEBAL derived instantaneous sensible (*H*) and latent (*LE*) heat fluxes estimates ($\overline{S}$) versus ground measurements ($\overline{G}$).

Scenario	Selection Anchor Pixel	Comments		n	$\overline{G}$ [6]	$\overline{S}$ [7]	SD_G	SD_S	r^2	MAD	RMSD	MRD
				(-)	(W/m^2)	(W/m^2)	(W/m^2)	(W/m^2)	(-)	(W/m^2)	(W/m^2)	%
S1	EC Approach (FP) [1]	-	H	25	262	156	151	105	0.76	108	131	40.4
			LE	25	299	314	174	170	0.90	39	57	-5.0
S2	EC Approach (TP) [2]	-	H	25	262	138	151	91	0.81	126	147	47.2
			LE	25	299	333	174	162	0.85	56	74	-11.5
S3	EM Approach	-	H	25	262	171	151	77	0.64	111	135	35.0
			LE	25	299	291	174	143	0.78	66	81	2.7
S4	EC Approach (TP)[3]	SEBAL R_n replaces ground R_n[4]	H	25	209	207	112	114	0.83	36	46	0.8
			LE	25	262	258	171	170	0.92	39	48	1.7
S5	EM Approach	SEBAL R_n replaces ground R_n[5]	H	25	205	171	110	77	0.59	61	77	16.6
			LE	25	257	291	167	143	0.82	61	77	-13.2

[1] Anchor pixels were selected by matching the instantaneous *LE* at the satellite overpass measured at the EC tower and the footprint weighted averaged SEBAL flux. [2] Anchor pixels were selected by matching the instantaneous *LE* at the satellite overpass measured at the EC tower and the SEBAL flux of the tower pixel. [3] Anchor pixels were selected by matching the instantaneous *LE* at the satellite overpass measured at the EC tower and the SEBAL flux of the tower pixel. In S4, the SEBAL estimated R_n replaces the R_n measured on the ground for adjustment of the latent heat flux. [4] Instead of using the R_n measurements made on the ground, the SEBAL derived R_n in Scenario 2 is used for the determination of the ground measured energy balance and in adjusting the *H* and *LE* from the EC for closure error (using Bowen ratio). [5] Instead of using the R_n measurements made on the ground, the SEBAL derived R_n in Scenario 3 is used for the determination of the ground measured energy balance and in adjusting the *H* and *LE* from the EC for closure error (using Bowen ratio). [6] The heat fluxes have been calculated from the EC measurements. Since no soil heat flux measurements were available for the Middle Rio Grande Basin, the SEBAL soil heat flux was used to establish the ground measured energy balance. [7] The SEBAL estimates of the instantaneous *H* and *LE* were obtained by calculating the footprint weighted averaged SEBAL heat fluxes.

Table 8. Quantitative measures for comparison of SEBAL derived daily sensible (H) and latent (LE) heat fluxes estimates ($\overline{S}$) versus ground measurements ($\overline{G}$).

$EF_{24} = 1.0 \times EF_{inst}$

Scenario	Selection Anchor Pixel		n	$\overline{G}$ [6]	$\overline{S}$ [7]	SD_G	SD_S	r^2	MAD	RMSD	MRD
			(-)	MJ/(m²d)	MJ/(m²d)	MJ/(m²d)	MJ/(m²d)	(-)	MJ/(m²d)	MJ/(m²d)	%
S1	EC Approach (FP) [1]	H	24	6.0	7.2	3.7	3.2	0.41	2.3	3.1	-19.4
		LE	24	9.1	8.9	4.4	4.9	0.78	1.7	2.2	2.9
S2	EC Approach (TP) [2]	H	24	6.0	6.9	3.7	3.3	0.32	2.6	3.3	-14.9
		LE	24	9.1	9.1	4.4	5.0	0.72	2.2	2.6	0.0
S3	EM Approach	H	24	6.0	7.6	3.7	2.7	0.37	2.6	3.3	-27.0
		LE	24	9.1	8.3	4.4	4.2	0.69	1.9	2.6	8.9

$EF_{24} = 1.1 \times EF_{inst}$

Scenario	Selection Anchor Pixel		n	$\overline{G}$ [6]	$\overline{S}$ [7]	SD_G	SD_S	r^2	MAD	RMSD	MRD
			(-)	MJ/(m²d)	MJ/(m²d)	MJ/(m²d)	MJ/(m²d)	(-)	MJ/(m²d)	MJ/(m²d)	%
S1	EC Approach (FP) [1]	H	24	6.0	6.3	3.7	3.5	0.41	2.1	3.0	-5.6
		LE	24	9.1	9.7	4.4	5.3	0.78	1.9	2.5	-6.3
S2	EC Approach (TP) [2]	H	24	6.0	6.0	3.7	3.6	0.32	2.7	3.3	-0.8
		LE	24	9.1	10.0	4.4	5.4	0.71	2.4	3.0	-9.3
S3	EM Approach	H	24	6.0	6.9	3.7	3.0	0.42	2.3	2.9	-14.8
		LE	24	9.1	9.2	4.4	4.6	0.69	2.0	2.5	-0.3

[1] Anchor pixels were selected by matching the instantaneous LE at the satellite overpass measured at the EC tower and the footprint weighted averaged SEBAL flux. [2] Anchor pixels were selected by matching the instantaneous LE at the satellite overpass measured at the EC tower and the SEBAL flux of the tower pixel. [5] Instead of using the R_n measurements made on the ground, the SEBAL derived R_n in Scenario 3 is used for the determination of the ground measured energy balance. [6] The heat fluxes have been calculated from the EC measurements. Since no soil heat flux measurements were available for the Middle Rio Grande Basin, the SEBAL soil heat flux was used to establish the ground measured energy balance.[7] The SEBAL estimates of the instantaneous H and LE were obtained by calculating the footprint weighted averaged SEBAL heat fluxes.

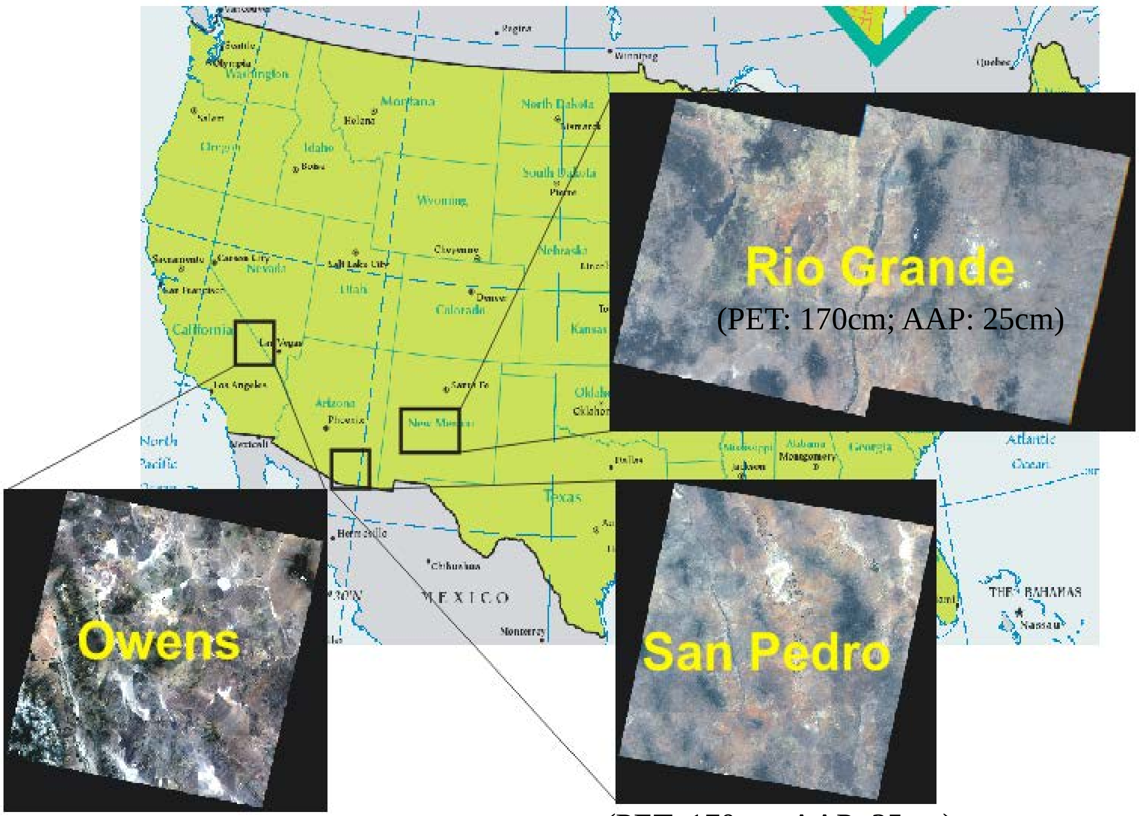

(PET: 150cm; AAP: 12cm)

(PET: 170cm; AAP: 35cm)

Figure 1 Landsat7 scenes of the study areas in New Mexico, Arizona and California. (PET: potential evapotranspiration; AAP: average annual precipitation)

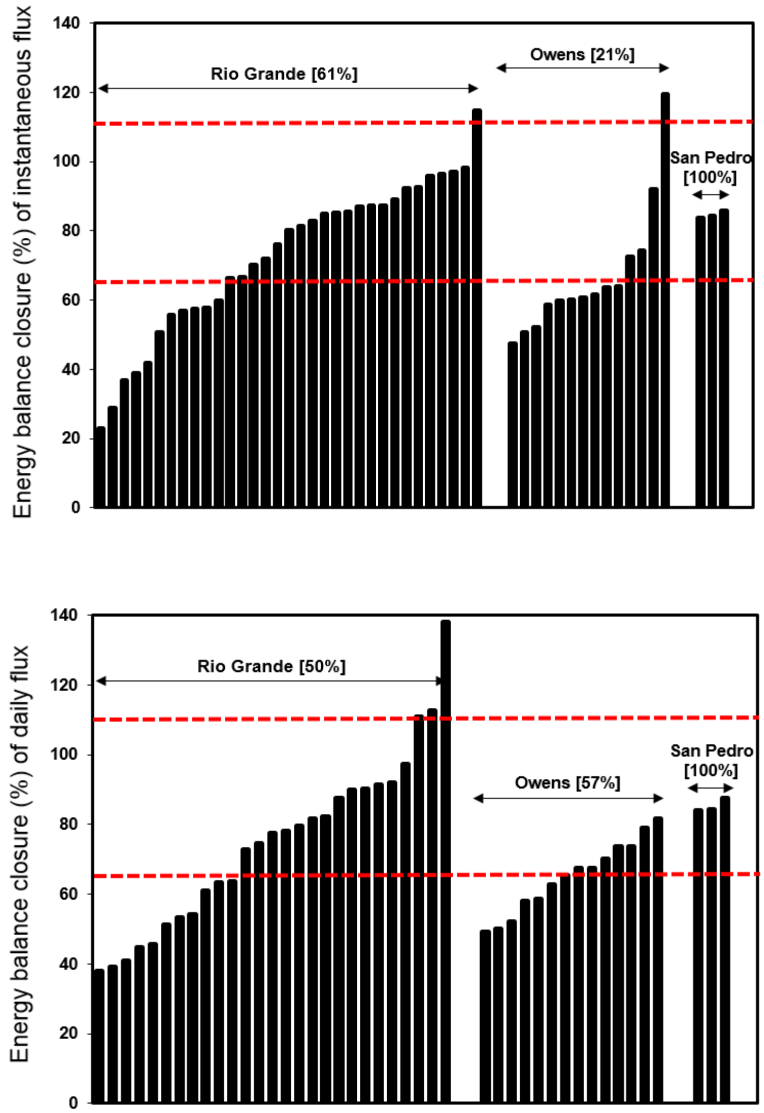

Figure 2. Distribution of energy balance relative closure $(H+LE)/(R_n–G)$ of instantaneous (top panel) and total daily (bottom panel) fluxes from eddy covariance towers. Each 'bar' represents a satellite overpass day. The dotted lines show criteria of acceptable closure [65 and 110 %] and percentage of the data having acceptable closure is shown in bracket.

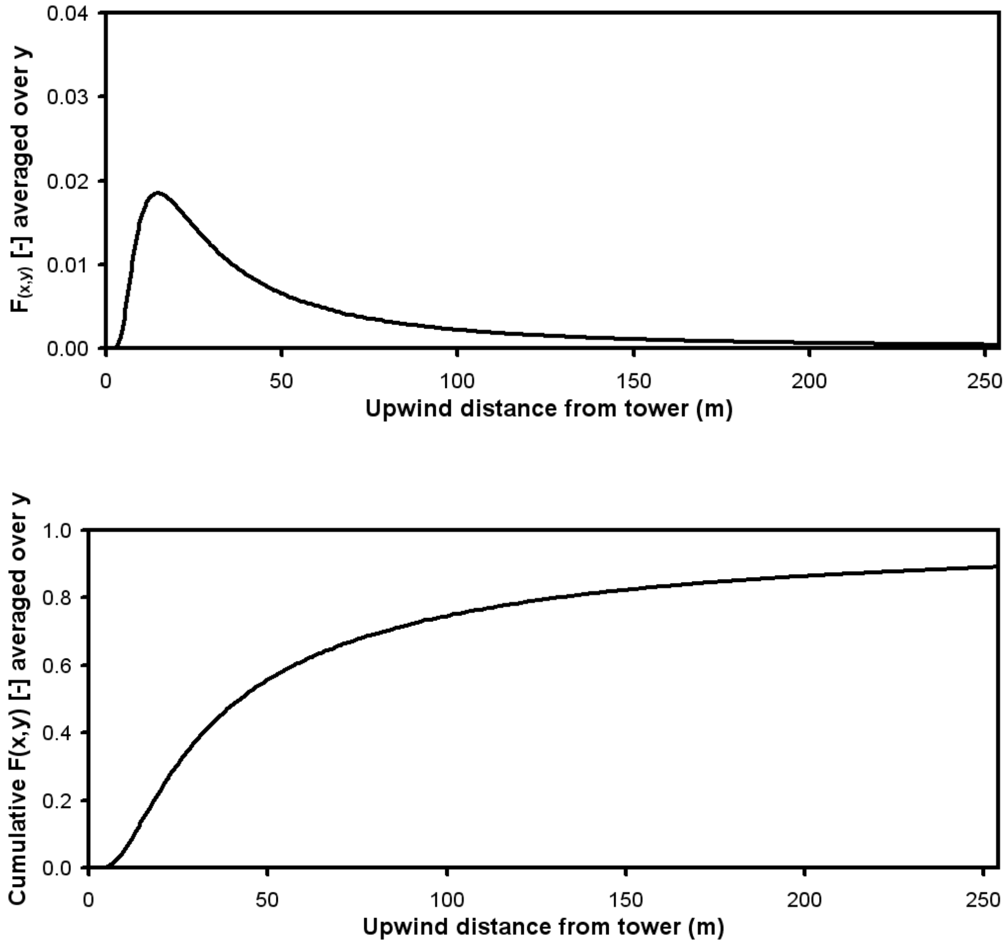

Figure 3. Footprint size and footprint intensity from the eddy covariance tower located at SEV (saltcedar) in Rio Grande on August 19, 2002 (10:40 am) (wind speed: 3.4 m/s, vegetation height: 4.9 m and sonic anemometer height from ground: 6.5 m).

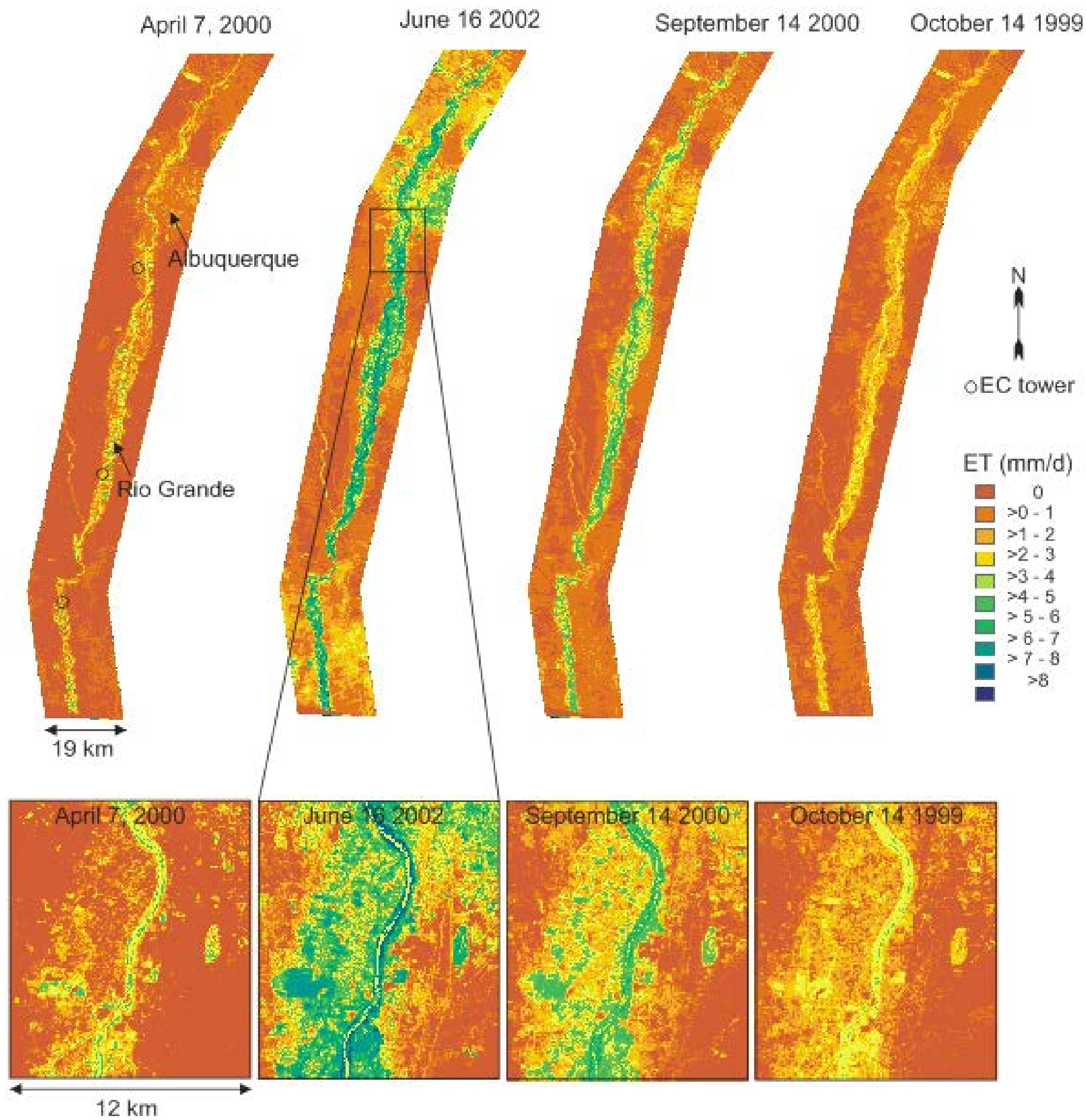

Figure 4. SEBAL daily evapotranspiration (mm/d) maps along the Rio Grande in spring, summer and fall.

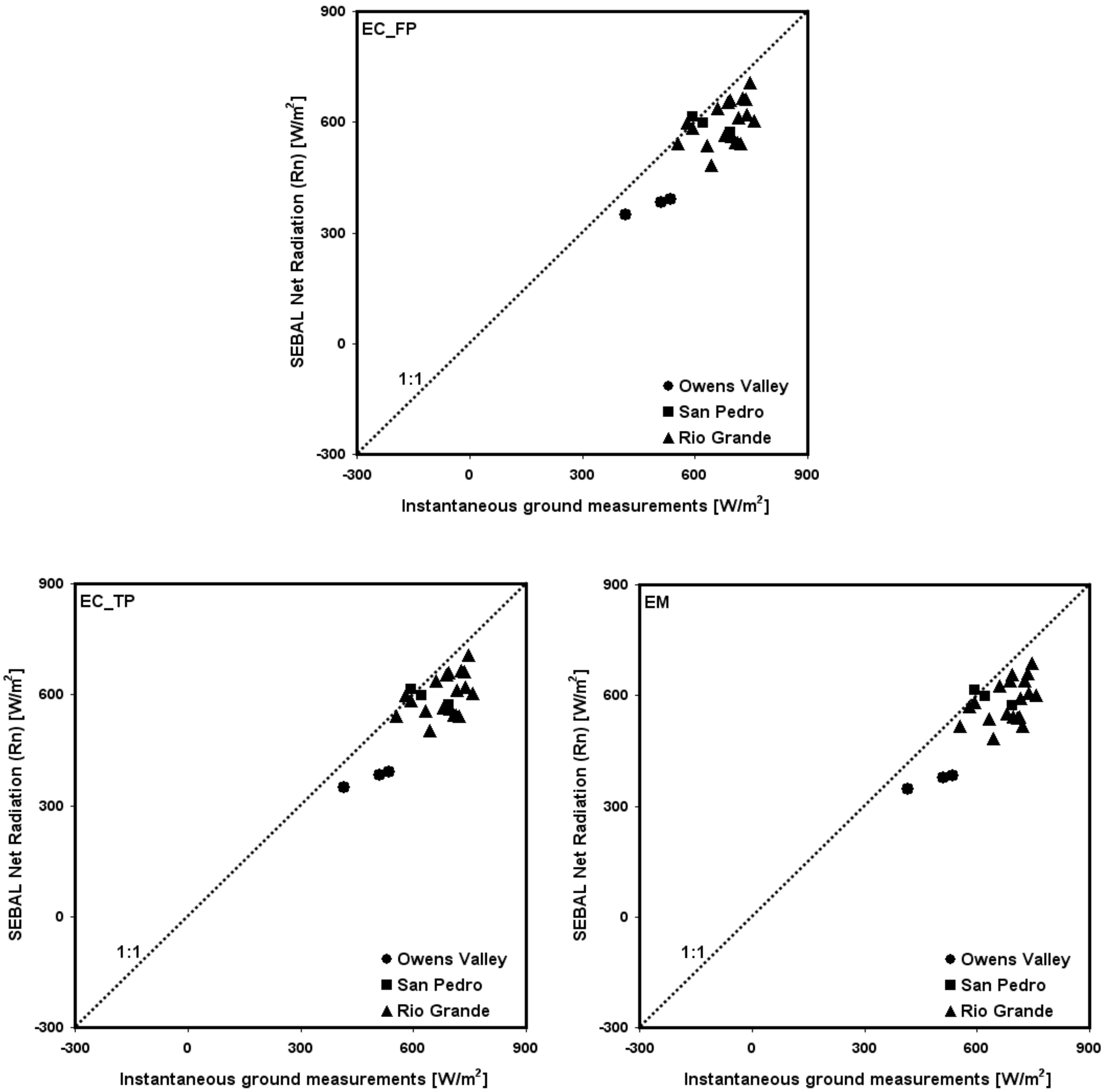

Figure 5. Comparison of instantaneous net radiation (R_n) between net radiometer measurements and SEBAL estimates. (EC_FP (S1) method selected anchor pixels to match fluxes of the ground measured instantaneous *LE* (adjusted for closure error) at the satellite overpass and the footprint weight averaged SEBAL *LE*. EC_TP (S2) method selected anchor pixels to match fluxes of the ground measured instantaneous *LE* and the flux of the tower pixel. EM (S3) method selected the anchor pixels with the hydrogeological features of the landscape and micrometeorological considerations.

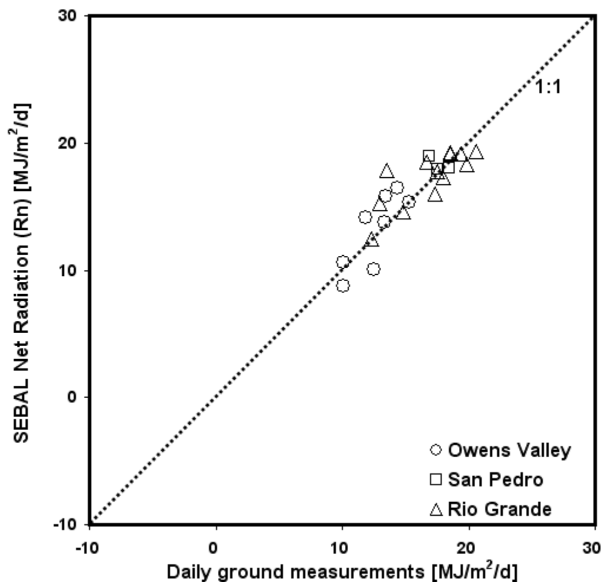

Figure 6. Comparison of daily net radiation (R_n) between net radiometer measurements and SEBAL estimates.

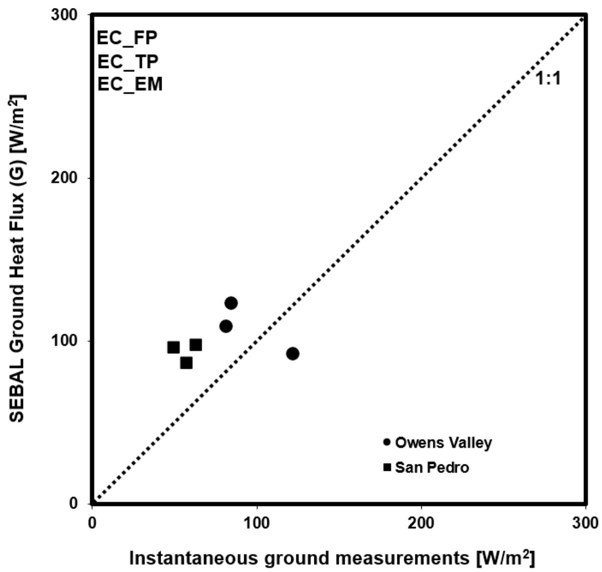

Figure 7. Comparison of instantaneous ground heat flux (*G*) between soil heat flux plate measurements and SEBAL estimates in Owens Valley and San Pedro Valley. EC_FP (S1) EC_TP (S2), and EM (S3) methods produced very similar SEBAL estimates.

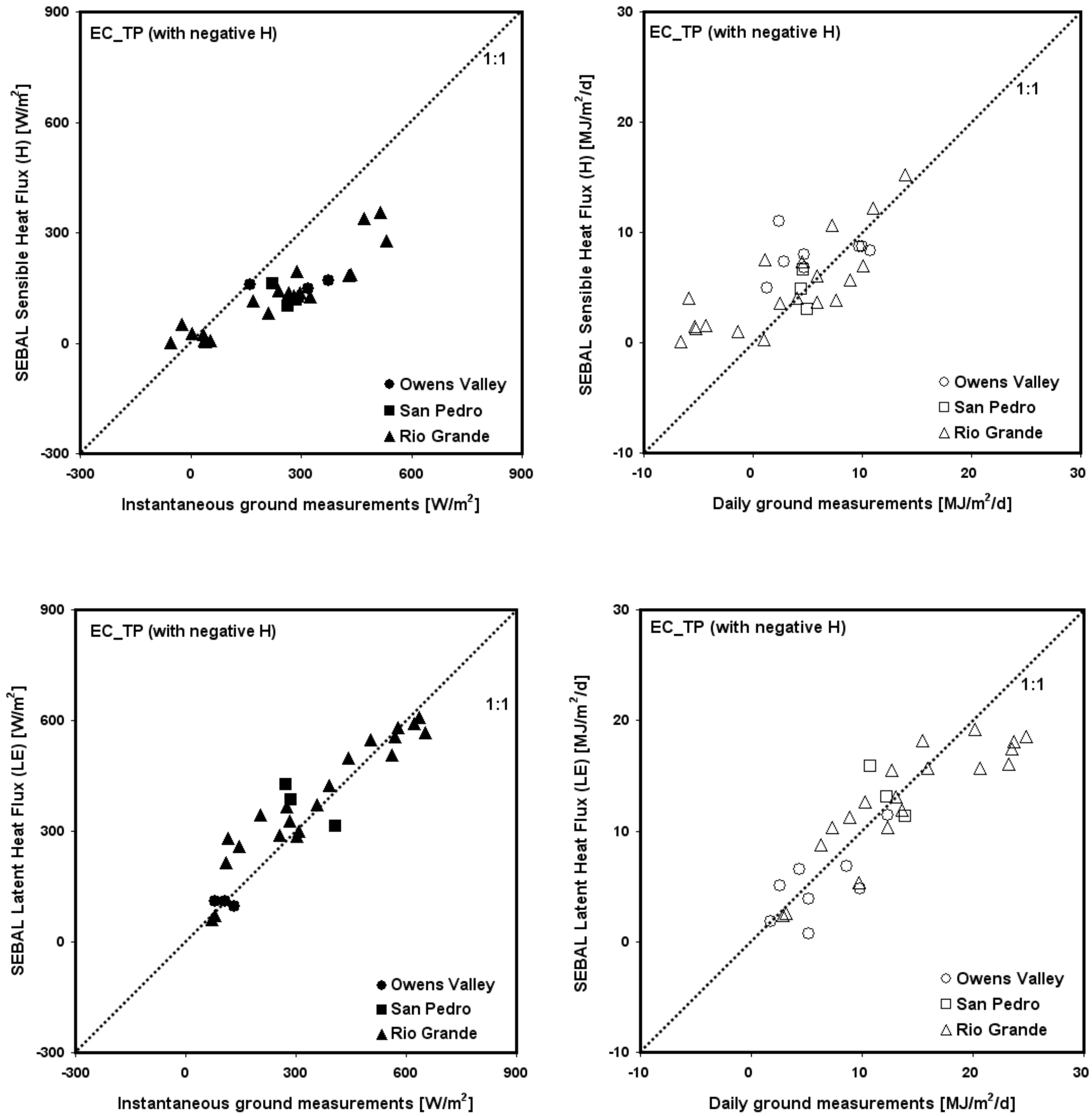

Figure 8. Comparison of sensible (*H*) and latent heat (*LE*) fluxes between adjusted eddy covariance tower measurements (with negative *H* data points) and SEBAL estimates from scenario S2 (EC_TP).

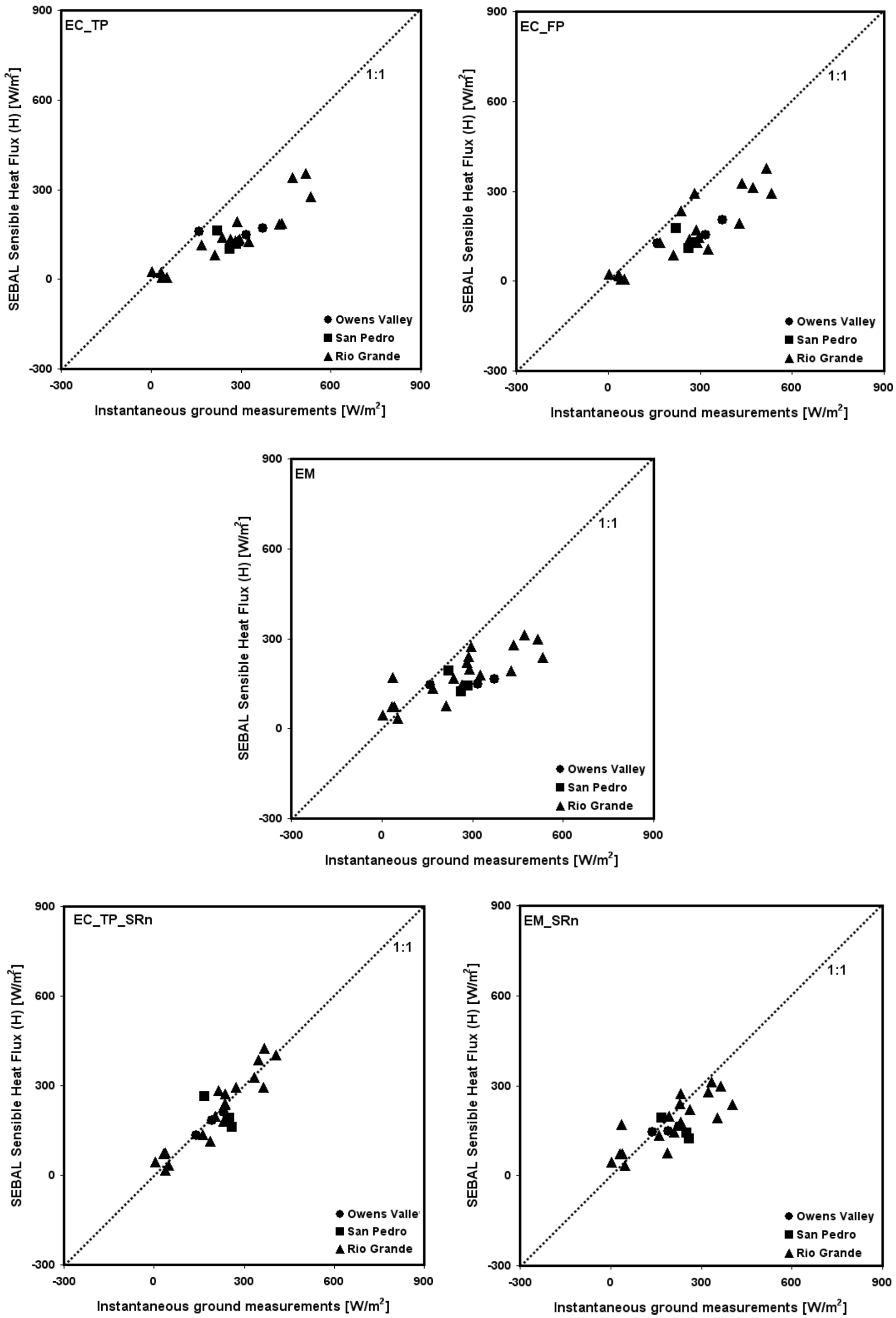

Figure 9. Comparison of instantaneous sensible heat flux (*H*) between adjusted eddy covariance tower measurements and SEBAL estimates for scenarios S1–S5.

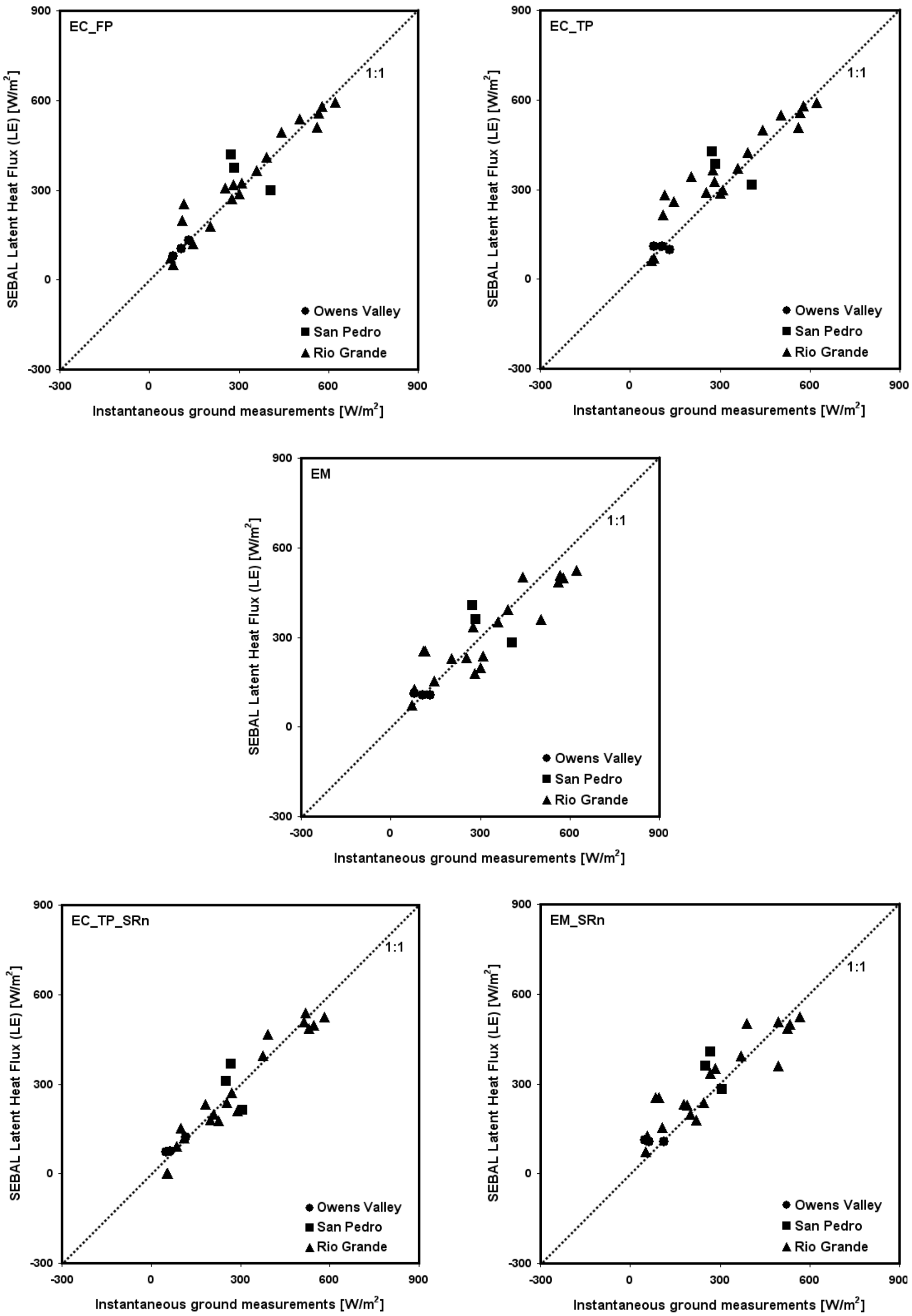

Figure 10. Comparison of instantaneous latent heat flux (*LE*) between adjusted eddy covariance tower measurements and SEBAL estimates for scenarios S1–S5.

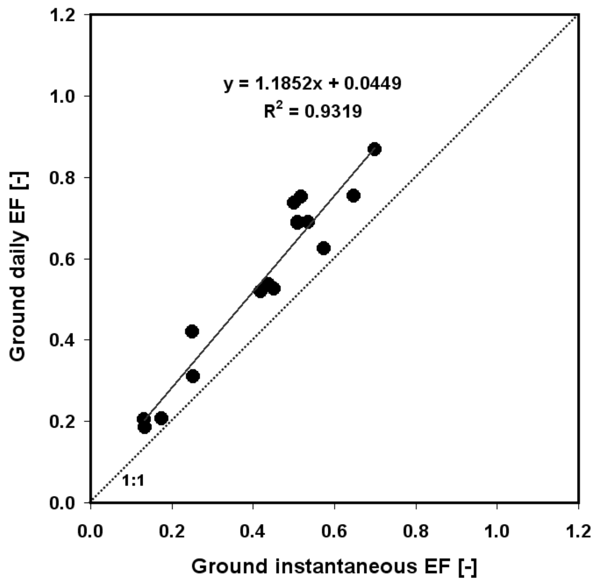

Figure 11. Comparison of satellite overpass instantaneous evaporative fraction (*EF*) with daytime average measured on the ground.

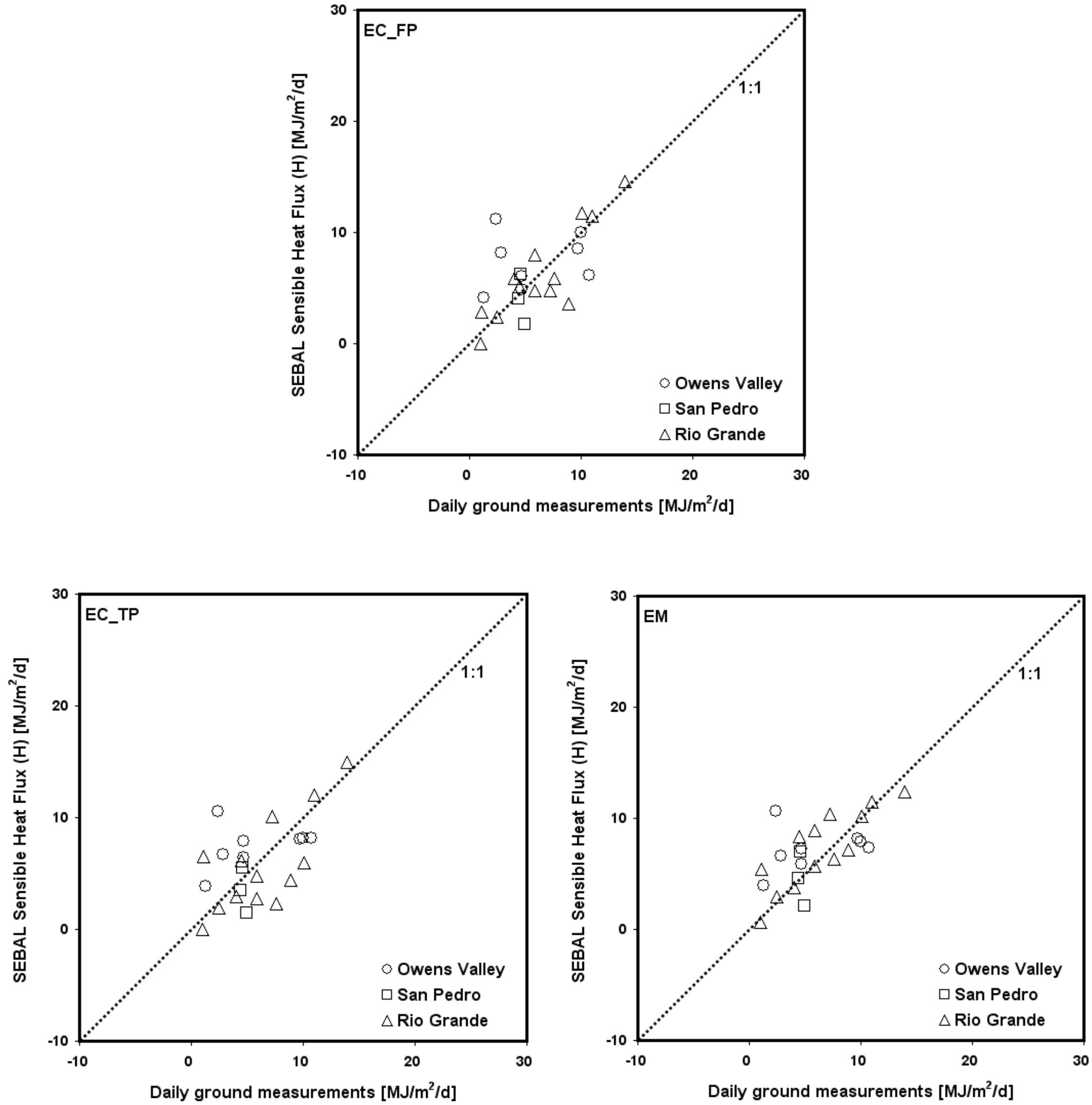

Figure 12. Comparison of daily sensible heat flux (*H*) between adjusted eddy covariance tower measurements and SEBAL estimates. ($EF_{24} = 1.1 * EF_{inst}$)

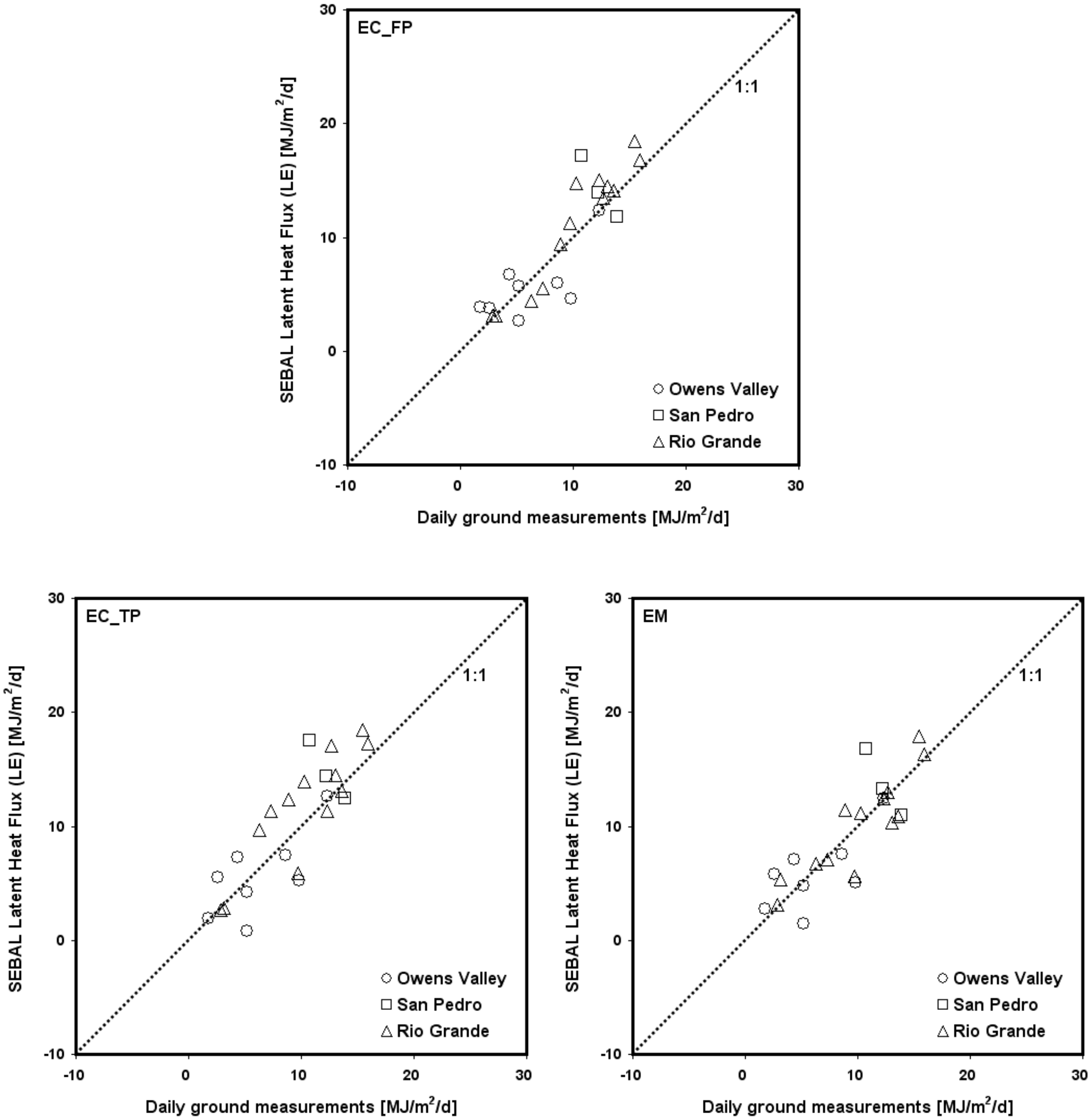

Figure 13. Comparison of daily latent heat flux (*LE*) between adjusted eddy covariance tower measurements and SEBAL estimates. ($EF_{24} = 1.1 * EF_{inst}$)

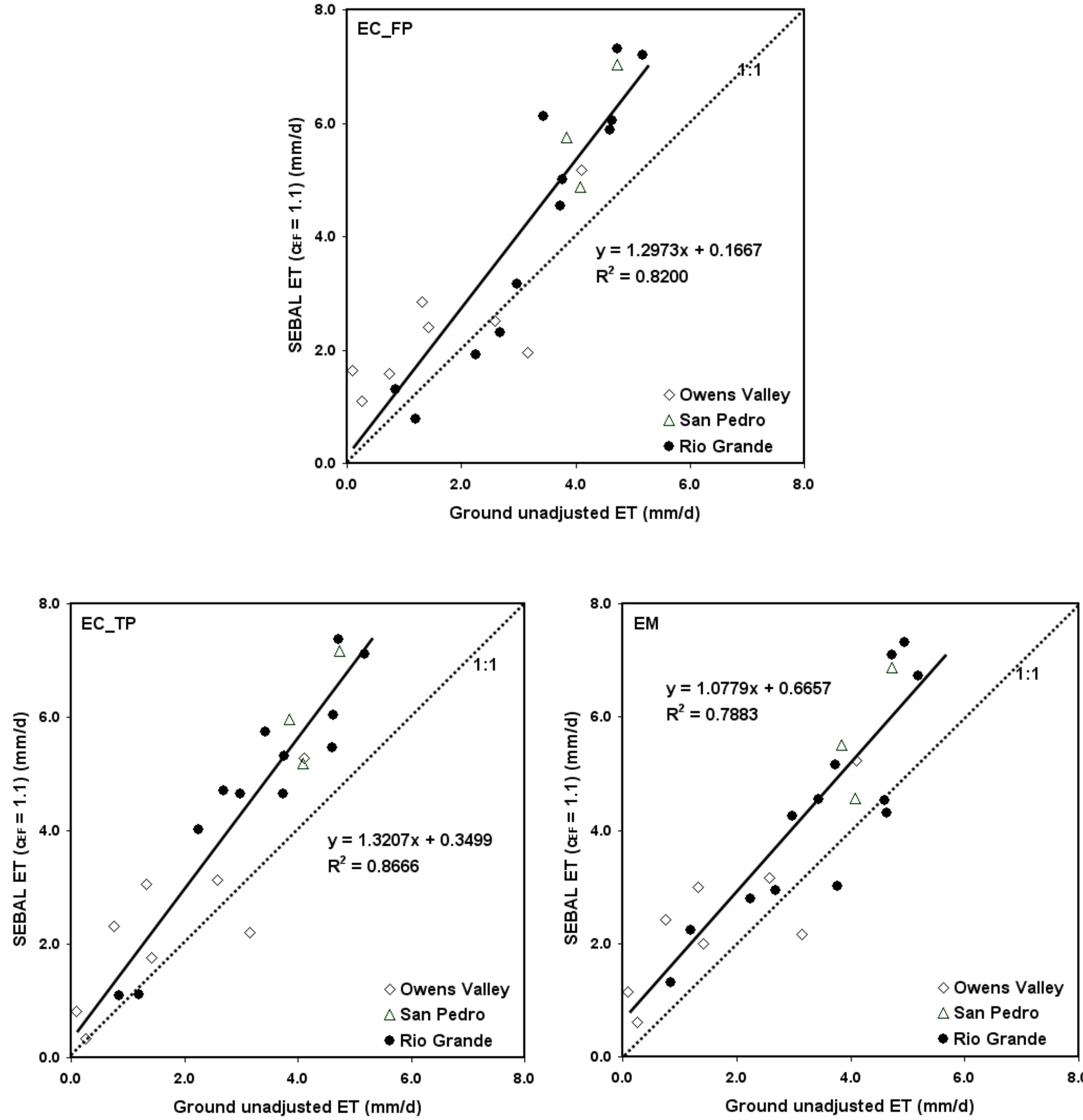

Figure 14. Comparison of ET rates determined from SEBAL with c_{EF} of 1.1 to eddy covariance ground measurements in riparian areas of the Rio Grande Valley (NM), San Pedro Valley (AZ), and Owens Valley (CA).